

K. J. Meissner · A. J. Weaver · H. D. Matthews
P. M. Cox

The role of land surface dynamics in glacial inception: a study with the UVic Earth System Model

Received: 22 January 2003 / Accepted: 31 July 2003 / Published online: 23 October 2003
© Springer-Verlag 2003

Abstract The first results of the UVic Earth System Model coupled to a land surface scheme and a dynamic global vegetation model are presented in this study. In the first part the present day climate simulation is discussed and compared to observations. We then compare a simulation of an ice age inception (forced with 116 ka BP orbital parameters and an atmospheric CO₂ concentration of 240 ppm) with a preindustrial run (present day orbital parameters, atmospheric [CO₂] = 280 ppm). Emphasis is placed on the vegetation's response to the combined changes in solar radiation and atmospheric CO₂ level. A southward shift of the northern treeline as well as a global decrease in vegetation carbon is observed in the ice age inception run. In tropical regions, up to 88% of broadleaf trees are replaced by shrubs and C₄ grasses. These changes in vegetation cover have a remarkable effect on the global climate: land related feedbacks double the atmospheric cooling during the ice age inception as well as the reduction of the meridional overturning in the North Atlantic. The introduction of vegetation related feedbacks also increases the surface area with perennial snow significantly.

1 Introduction

At the end of the last interglacial (120–115 ka BP), proxy data for the global ice volume on Earth indicate a sudden increase of inland ice along with a global sea level drop of about 50 m in 10,000 years (Shackleton 1987). The causes for this dramatic climate change are

still subject to debate. Although it is widely accepted that changes in solar radiation and its geographical and seasonal distribution are triggers for ice age inceptions (astronomic theory of glaciation, Milankovitch 1930), changes in the Earth's orbital parameters without prejudice to the climate mechanisms actually involved are not sufficient to explain the observed glacial cycles (Crowley and North 1991). Positive feedbacks in the climate system must therefore be considered as amplifiers of the external forcing (Broecker and Denton 1990).

Over the last 20 years, several model studies of varying complexity have investigated these positive feedbacks and their role during ice age inceptions (see Yoshimori et al. 2002 for a detailed overview). The simulation of an ice sheet nucleation and growth rate in agreement with paleodata has been met with varying degrees of success: Royer and Deque (1983) and Royer et al. (1984) were the first studies carried out with an atmospheric general circulation model (AGCM). These studies changed only the orbital parameters and the occurrence of permanent snow cover over ice sheet nucleation sites was not addressed. Five years later, Rind et al. (1989) carried out several experiments under varying orbital parameters, sea surface temperature (SST) patterns and atmospheric CO₂ concentrations. Perennial snow cover only occurred under full glacial ocean conditions and when 10 m of land ice were specified over the areas of the CLIMAP Last Glacial Maximum (LGM) ice sheets (CLIMAP Project Members 1981).

In the early 1990s, Oglesby (1990) and Verbitsky and Oglesby (1992) discussed the importance of reduced atmospheric CO₂ concentrations for ice sheet growth. A positive net snow accumulation was found under the condition of very low atmospheric CO₂ concentrations (100 ppm) or by imposing an initial 1 m snow cover over the entire Northern Hemisphere (Oglesby 1990). The areas of net snow accumulation, however, were in

K. J. Meissner (✉) · A. J. Weaver · H. D. Matthews
School of Earth and Ocean Sciences, University of Victoria,
Victoria, Canada
E-mail: katrin@ocean.seos.uvic.ca

P. M. Cox
Hadley Centre, Meteorological Office, Bracknell, UK

conflict with geological data for ice sheet nucleation sites. Using an ice sheet-asthenosphere model, Verbitsky and Oglesby (1992) found the simulated maximum ice volume an order of magnitude smaller than estimates derived from sea level records.

Several simulations under extreme orbital configurations were conducted by Philipps and Held (1994) and Gallimore and Kutzbach (1995). Their main conclusion was that orbital forcing alone cannot account for permanent snow cover in North America and Europe. Sytkus et al. (1994), Schlesinger and Verbitsky (1996) and Dong and Valdes (1995) considered the combination of orbital and CO₂ forcing. While Sytkus et al. (1994) found a critical threshold value of atmospheric CO₂ for ice sheet nucleation, Dong and Valdes (1995) and Schlesinger and Verbitsky (1996) were successful in simulating ice sheet growth under changed orbital and CO₂ forcing. However, the simulated global ice volume in the latter study was only a third of the estimate derived from sea level records. The simulated perennial snow in Dong and Valdes (1995) covered most of the high latitudes including Alaska, which is in conflict with geological data that indicates no early ice in those areas (Clark et al. 1993).

One serious problem that climate models encounter while simulating mass balances on ice sheets from AGCM simulations is related to the spatial resolution. Dynamic ice sheet models and the underlying bedrock topography need a higher horizontal resolution than AGCMs can provide. Simulations including subgrid topographic information have been carried out by Pollard and Thompson (1997) and Marshall and Clarke (1999). A table comparing former model studies cited here as well as a very detailed description of the different results can be found in Yoshimori et al. (2002).

The response of boreal vegetation during ice age inception is one of the most important positive feedbacks in the climate system that may be able to amplify the orbital forcing. Snow covered tundra or grass areas are characterized by a higher albedo than snow covered forests (~ 0.8 versus ~ 0.4), as trees mask the snow efficiently such that the albedo is considerably lowered (Federer 1968; Betts and Ball 1997; Crucifix and Loutre 2002). The southward migration of the treeline due to cooler climate conditions thus leads to a higher surface albedo which reflects more incoming shortwave radiation and acts to enhance the initial cooling.

Several model studies have included this vegetation feedback: Gallimore and Kutzbach (1996) coupled an AGCM with a mixed layer ocean model to study the influence of two different scenarios of tundra expansion; de Noblet et al. (1996) integrated a global equilibrium biome model iteratively with an AGCM to study the role of a biogeophysical feedback in initiating glaciations; Pollard and Thompson (1997) also conducted an AGCM experiment with a dynamic ice sheet model and an interactively coupled vegetation model; Yoshimori et al. (2002) studied the influence of two different tundra

expansion scenarios and two different sea surface conditions during ice age inception runs conducted with an AGCM. None of these studies, however, included the terrestrial biosphere as a dynamic element of the climate system. The vegetation cover during ice inception was either prescribed (Gallimore and Kutzbach 1996; Yoshimori et al. 2002) or the result of simulations with equilibrium terrestrial biosphere models (de Noblet et al. 1996; Pollard and Thompson 1997).

To fully understand the role of climate-vegetation feedbacks during important climate changes, the terrestrial biosphere must be treated as a dynamically interactive element of the climate system. To make such fully coupled interactive simulations possible, dynamic global vegetation models (DGVMs) have been developed during the last 10 years (Friend et al. 1993; Post and Pastor 1996; Foley et al. 1996; Cox 2001). However, these models have mostly been applied in offline studies, which neglect climate-biosphere feedbacks. There is an urgent need to assess the role of such feedbacks in the climate system, which requires the inclusion of DGVMs within the full Earth System models.

Crucifix and Loutre (2002) are pioneers in investigating the feedbacks and forcings during the last interglacial period with an earth system model of intermediate complexity called 'MoBidiC' that combines many of the climate system's important subcomponents. Their model consists of a zonally-averaged atmospheric model, a sectorially-averaged multi-level ocean model, a simple thermodynamic-dynamic sea ice model and the dynamical vegetation model VECODE developed by Brovkin et al. (1997). Some of their conclusions regarding the ice age inception involve a southward shift of the northern treeline by 14° in latitude as well as important changes in summer sea ice and summer snow. These environmental changes cause variations in surface albedo that nearly quadruple the direct effect of the astronomical forcing. Lacking a continental ice sheet model, ice sheet nucleation and growth could not be represented by Crucifix and Loutre (2002).

In this study, we pursue two aims: first we will introduce the land surface scheme and vegetation model, two new components of our Earth system model. The model description (Sect. 2 and Appendix 1) will be followed by a discussion of the results from a present day control run (Sect. 3). Second, we investigate the vegetation's and ocean's response to an ice age inception scenario with our fully coupled atmosphere-ocean-land surface-vegetation-sea ice model (Sect. 4). All simulations presented in this study are in statistical equilibrium, showing the equilibrium vegetation for a given climate. Conclusions are given in Sect. 5.

2 Model description

The UVic Earth System Climate Model (ESCM) consists of an ocean general circulation model (Modular Ocean Model, Version 2, Pacanowski 1995) coupled to a vertically integrated two

dimensional energy-moisture balance model of the atmosphere, a dynamic-thermodynamic sea ice model (Bitz et al. 2001), a new land surface scheme and a dynamic global vegetation model (Cox et al. 2000). The model version including the atmospheric, ocean and sea ice model is described in Weaver et al. (2001). It is driven by seasonal variations in solar insolation at the top of the atmosphere and seasonally varying wind stress at the ocean surface (Kalnay et al. 1996). All experiments presented here are computed with near surface advection of specific humidity as described in Weaver et al. (2001). The wind field used for moisture advection is a weighted average of long term climatological monthly means from all of the NCEP atmospheric levels available up to about 10,000 m (Kalnay et al. 1996). Each level is weighted as a negative exponential function of its height to reflect the exponential decrease of water vapor as a function of height. The distribution of water vapor as function of height has also been considered in the calculation of saturated moisture and diffusive water vapor transport over mountains. For a realistic simulation of precipitation over land areas and since our use of specified winds does not account for transient eddies, we increase linearly from the coast the zonal diffusion coefficient for water vapor transport over important land masses (i.e. Asia) by an amount relative to the distance from the coast. This new parametrization and its effects on the precipitation rates are discussed in Sect. 3. The new components of the UVic ESCM, a land surface scheme and vegetation model are described in Sect. 2.1 and in Appendix 1.

2.1 Vegetation model and land surface scheme

The dynamic global vegetation model (DGVM) called ‘TRIFFID’ (Top-down Representation of Interactive Foliage and Flora Including Dynamics) was developed at the Hadley Centre for use in coupled climate-carbon cycle simulations (Cox et al. 2000) and is described in Cox (2001). TRIFFID defines the state of the terrestrial biosphere in terms of soil carbon, and the structure and coverage of five plant functional types (PFT): broadleaf tree, needleleaf tree, C₃ grass, C₄ grass and shrub. The areal coverage, leaf area index and canopy height of each PFT are calculated based on a ‘carbon balance approach’, in which vegetation change is driven by net carbon fluxes. These fluxes are derived for each vegetation type using the coupled photosynthesis-stomatal conductance model developed by Cox et al. (1999b), which utilizes existing models of leaf-level photosynthesis in C₃ and C₄ plants (Collatz et al. 1991, 1992). TRIFFID is coupled to a land surface scheme described in Appendix 1. This land surface scheme improves on the simple land surface model used in Matthews et al. (2003) by including a better representation of evapo-transpiration (a function of canopy resistance), surface albedo (a function of vegetation type and leaf area index) and runoff.

2.2 Coupling

The land-atmosphere fluxes, runoff and carbon fluxes are calculated within the land surface scheme every 6 h and time-averaged before being passed to the atmospheric and ocean model (every 2.5 days) and to TRIFFID (every month). TRIFFID allocates the average net primary productivity over this coupling period into the growth of the existing vegetation and to the expansion of the ‘vegetated area’. Leaf phenology is updated on an intermediate time scale of 1 day, using accumulated temperature-dependent leaf turnover rates. The land surface parameters, dependent on the type, height and leaf area index of the vegetation (e.g. albedo, roughness length), are updated after each call to TRIFFID. Radiation, heat fluxes and precipitation rates are calculated and time-averaged within the atmospheric model before being passed to the land surface scheme every 2.5 days. The coupling between the atmosphere, ocean, sea ice, land surface and vegetation components is done without any ‘flux-adjustments’: freshwater (moisture) and energy are conserved to machine precision.

3 Present day control run

Since the sensitivity of the model climate ultimately depends on the model’s climate state itself, the importance of properly simulating the present day climate is paramount. We therefore begin our discussion with the model’s representation of present day climate under present day climatological wind fields and present day solar radiation. Present day croplands are prescribed from Ramankutty and Foley (1999), allocating areas where only C₃ and C₄ grasses are allowed to grow. Urban areas and lakes are not taken into account.

A first equilibrium run is obtained after more than 2000 years of integration with an atmospheric CO₂ concentration equal to 365 ppm (PD_EQ_LV run). In this simulation the model predicts a global total of 887 Gt of vegetation carbon, which is 35% more than estimates for the present day (654 GtC – including all anthropogenic land cover changes, Mooney et al. 2001). A possible explanation for this discrepancy is the fact that the model simulates an equilibrium vegetation for an atmospheric CO₂ concentration equal to 365 ppm. In the real world, the vegetation is in a transient phase and is still adapting to elevated CO₂ levels due to anthropogenic emissions.

To take this transient behavior of the climate system into account, we integrated the climate model to equilibrium under preindustrial conditions (atmospheric CO₂ concentration equal to 280 ppm). During the last 150 years of integration, an exponential increase of atmospheric CO₂ from 280 ppm to 365 ppm was imposed. Results from this transient run (called PD_LV run hereafter) are then compared to observations. Table 1 gives an overview of all simulations described in the present study.

The simulated global vegetation carbon equals 752 GtC and is at the high end of the range of estimates (Prentice et al. 2001). It is likely that anthropogenic land cover change can account for part of this remaining discrepancy. In this simulation only agricultural areas are specified (from Ramankutty and Foley 1999). Deforestation, pasture, urban areas and lakes are not considered here leading to a higher vegetation cover than in observations. With 15% more vegetation, the simulated global gross primary productivity (GPP: 184 GtC per year), net primary productivity (NPP: 83 GtC per year) and plant respiration (101 GtC per year) are also higher than present day estimates (120 GtC per year, 60 GtC per year and 60 GtC per year, respectively, Houghton et al. 2001). The simulated global carbon stocks in the soil are smaller than today’s estimates (1100 GtC versus 1600 GtC). However, these estimates include peatlands (~400 Gt), for example, which cannot be assessed with our very simple land surface scheme. The simulated global heterotrophic respiration amounts to 82 GtC per year (today’s estimates range from 68 to 77 GtC per year, Schlesinger and Andrews 2000).

Table 1 Description of the model runs

Simulation	Vegetation model	Orbital parameters	CO ₂ for atmosphere	CO ₂ for vegetation	anthropogenic land cover change	new parametrization for moisture transport
PD_EQ	No	PD	365	–	–	No
PD_M_TRANSP	No	PD	365	–	–	Yes
PI	No	PD	280	–	–	No
116 ka BP	No	116 ka BP	240	–	–	No
PD_EQ_LV	Yes	PD	365	365	Yes	Yes
PD_LV	Yes	PD	280 to 365	280 to 365	Yes	Yes
PI_LV	Yes	PD	280	280	No	Yes
116 ka BP_LV	Yes	116 ka BP	240	240	No	Yes
PI_240_LV	Yes	PD	280	240	No	Yes

The areal coverage of the five PFTs in the PD control run (PD_LV) are displayed in Fig. 1; the correlation between areal coverage of different plant functional types with IGBP (International Geosphere–Biosphere Programme, Loveland and Belward 1997) data is shown in Fig. 2 (please refer to Appendix 2 for a description on how the IGBP biomes have been converted into PFTs and how the correlation has been calculated). Some of the discrepancy can be explained by land cover changes that are not included in this model. For example, deforestation is only taken into account if replaced by crop land. In regions where urban areas took the place of forests or where deforestation is not replaced by agriculture, the model simulates a higher tree coverage than can be seen in observations. This leads to an overestimation of the distribution of broadleaf trees in western and eastern North America, southern South America and southern Africa (Fig. 1a). On the other hand, the fraction of broadleaf trees in Europe is underestimated: the simulated vegetation in this region consists mainly of needleleaf trees and C₃ grasses. The areal coverage of needleleaf trees is concentrated in northern North America and northern Europe and Asia (Fig. 1b), in good agreement with observations. However, the simulated atmospheric temperatures for our control run over northeast Asia and northeast North America are up to 10 °C higher than in observations (see Fig. 3a). As a result, the treeline in eastern Asia and eastern North America is up to 10 degrees too far north.

The simulated distribution of C₃ grasses is in excellent agreement with observations. They can be found in the European, Asian and North American cereal belts as well as in southern South America and southern Australia (Fig. 1c). C₃ grasses and shrubs are also simulated in northern North America and northern Asia as a representation of tundra. The model fails to represent C₃ grasses in southeast China. The distribution of C₄ grasses is concentrated in the Sahel zone, northern Australia, the Asian high plateaus and South America (Fig. 1d). The agreement with observations is high in Africa, Australia and western South America. Finally, shrubs are simulated in East Africa, eastern South America, the Himalayas region, northwest Australia and in the Eastern Indies. Discrepancies with observations

are located in the Eastern Indies, where one would expect broadleaf trees, and in eastern South America (broadleaf trees and C₄ grasses). Shrub is one of the PFTs that represents tundra in this model, with the result that large regions of northern Asia, Europe and North America are covered with shrubs as well (Fig. 1e).

Figure 1f shows that deserts are simulated in the right locations, but the Sahara is too small (extending only to 15°N) and the Australian desert is located too far east. The Gobi desert is slightly too big and the model simulates a small desert in southeastern China, non-existent in the real world.

The global correlation with IGBP data is 0.635 which is comparable to results obtained with TRIFFID coupled to an atmospheric general circulation model (AGCM). The worst agreement with data occurs in northern Asia and northern North America, where tundra is represented by C₃ grasses and shrubs (Fig. 2). As physiological responses are always more complex (and biome specific) than global vegetation models can represent, the description of tundra in terms of C₃ grasses and shrubs is necessarily simplified. However, C₃ is the predominant photosynthetic pathway and dominates in most locations except in the warm and dry tropics (or where C₄ crops like maize are grown). The plants in the tundra regions use the C₃ pathway, and tundra is made up of grasses and shrubs. The fact that the boreal treeline is reasonably well represented supports the view that this idealized treatment of the boreal forest/tundra competition is adequate for the purpose of coupling to a climate model. Southeastern China is too dry and is thus another region in poor agreement with IGBP data. The third important area with an agreement of less than 50% is located in western North America (south of the present United States and Mexico), where the model simulates broadleaf trees instead of C₄ grasses and shrubs, as a result of too much precipitation in this region.

As in the control runs without the vegetation model (Weaver et al. 2001), the equilibrium present day atmospheric temperature shows some discrepancies with the annually averaged NCEP (National Centers for Environmental Prediction) reanalysis climatology (Kalnay et al. 1996) over land (see Fig. 3a). Antarctica and most high elevation regions are cooler than NCEP

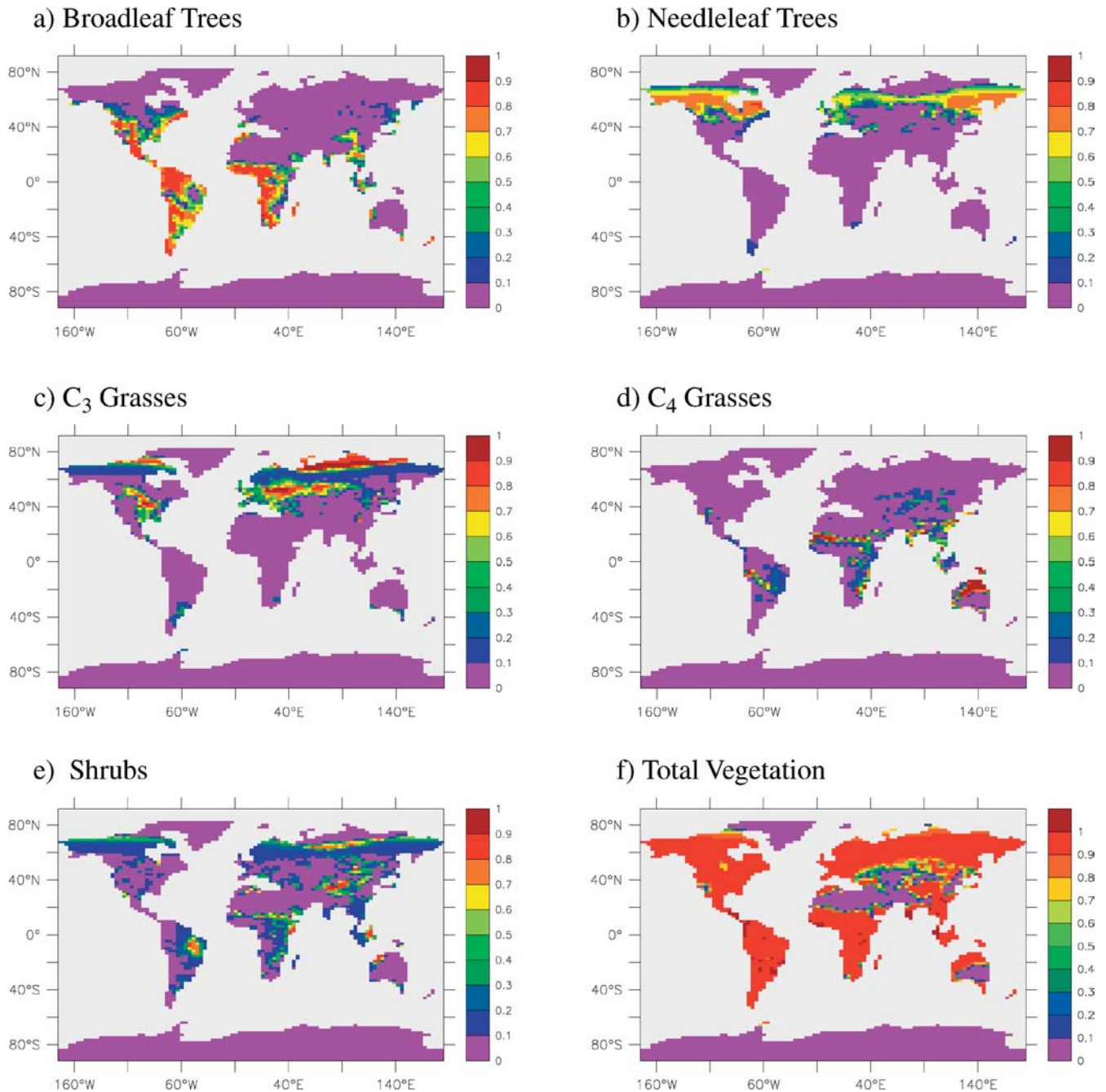


Fig. 1 Annually averaged areal coverage of **a** broadleaf trees, **b** needleleaf trees, **c** C_3 grasses, **d** C_4 grasses, **e** shrubs and **f** total vegetation simulated during the present day control run (PD_LV)

while the northeast coast of North America and Asia are warmer. The use of a constant atmospheric lapse rate ($6.5^\circ\text{C km}^{-1}$) as well as the lack of atmospheric dynamics likely contribute to these discrepancies. Over the ocean, the North Atlantic is cooler compared to observations, due to a slightly more extensive sea ice extent than is observed in this region (Weaver et al. 2001). The latter arises from the fact that North Atlantic Deep Water (NADW) formation sites are located too far south, as is common in most global ocean GCMs with coarse resolution. Some of these anomalies are reflected

in the simulated vegetation (e.g. treeline too far north in Eastern Asia and eastern North America). Such a bias in the present day simulation might be important during glacial inception simulations, since the error presumably also occurs during 116 ka BP simulations, and thus may provide a larger high latitude area over which the snow masking feedback can operate. Similar influences of basic-state errors on the strength of albedo feedback have been found regarding sea ice cover (Meehl and Washington 1990). On the other hand, these regions are warm biased (especially over the Laurentide ice sheet

Fig. 2 Agreement of the present day control simulation (PD_LV) with IGBP data (annual mean areal coverage of plant functional types)

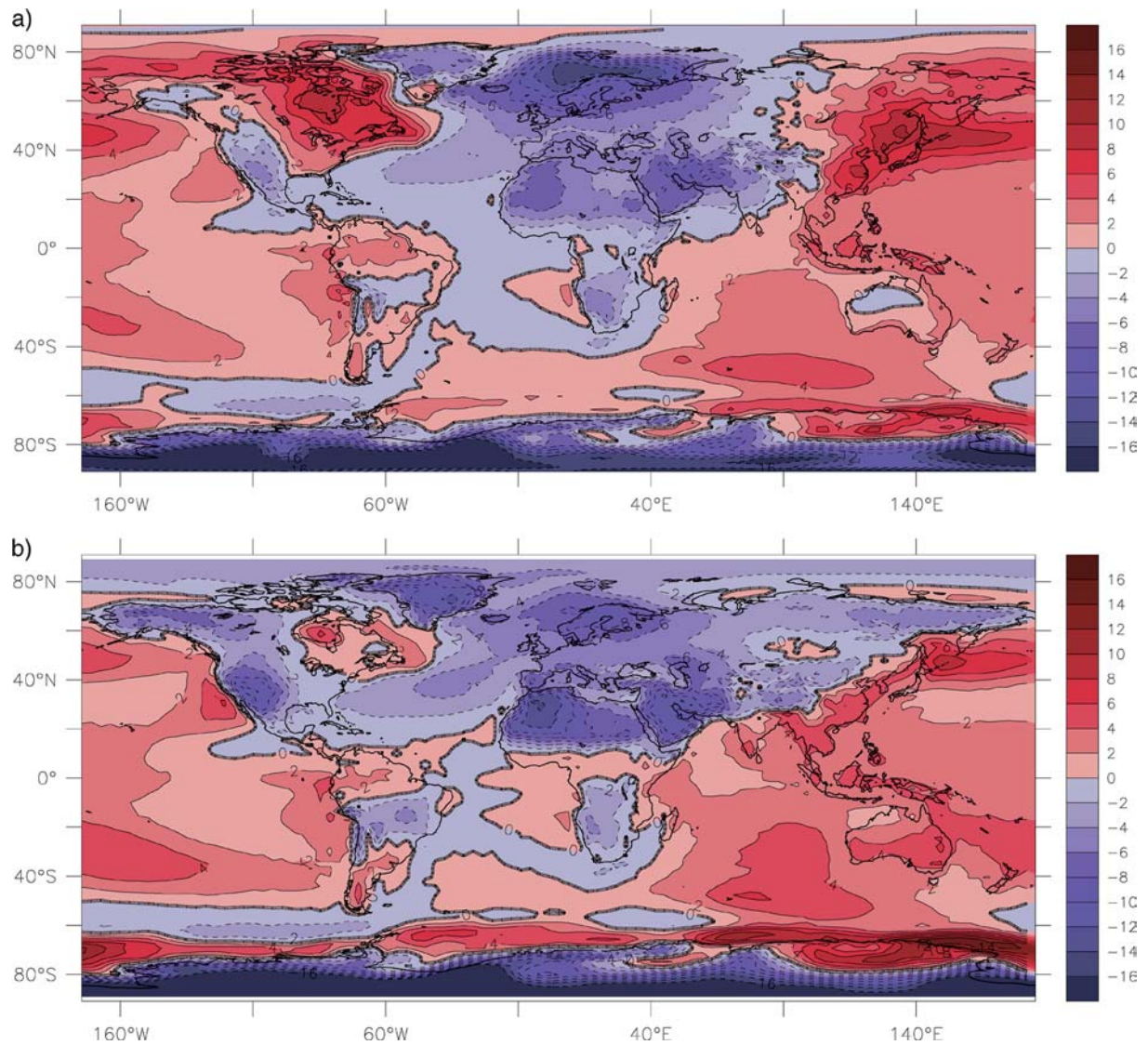
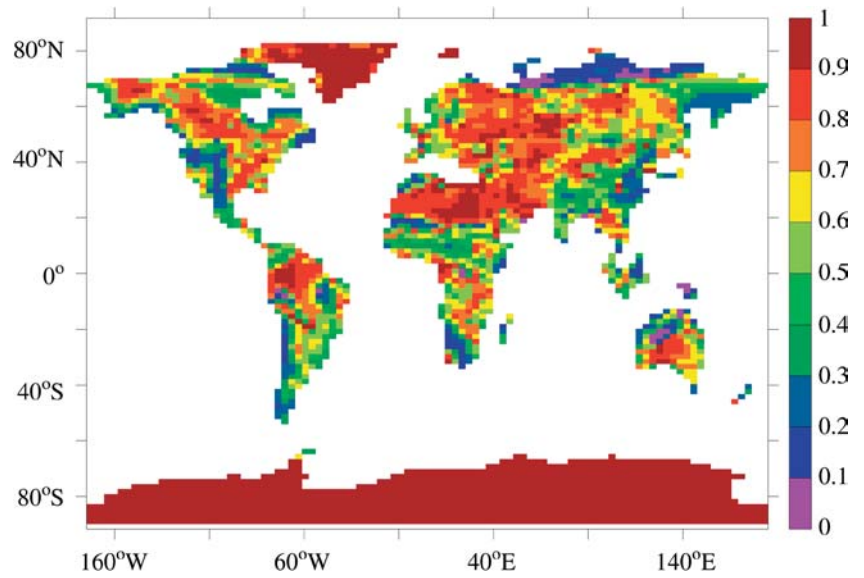


Fig. 3 Atmospheric surface temperature in °C, model (PD_LV) minus NCEP climatology **a** annual mean, **b** average over June, July and August

nucleation sites) and might hamper the simulation of local cooling and accumulation of perennial snow. However, the warm bias is less pronounced during the summer months: the simulated temperature is too cold over large parts of the Northern Hemisphere (Fig. 3b). A positive anomaly of 2 to 6 °C can only be seen over eastern Canada.

The parametrization of moisture transport in the atmosphere has been improved since the model version described by Weaver et al. (2001). Instead of using surface wind fields for moisture advection, the wind field used in this study is a weighted average of long term climatological monthly means from all of the NCEP atmospheric levels available up to about 10,000 m (Kalnay et al. 1996). The distribution of water vapor as function of height has also been considered in the calculation of saturated moisture and diffusive water vapor transport over mountains. The purpose of these changes was to increase the water transport over mountains and thus to increase precipitation rates over continents, which were too weak in the uncoupled model (Weaver et al. 2001).

Earlier simulations with the vegetation model using this new parametrization showed that continents (and especially Asia) were still too dry to simulate a realistic vegetation cover. To address this issue, we increased the zonal diffusion coefficients for water vapor transport linearly from the coast over important land masses (i.e. Asia) by an amount relative to the distance from the coast. Changing the diffusion coefficients had an important effect on the vegetation in Asia (namely the boreal forest). To quantify these changes in the parametrization of moisture transport, we run a present day equilibrium run with the uncoupled model using the new parametrizations (PD_M_TRANSP). Figure 4a shows the effect of the new parametrization on the uncoupled model (PD_M_TRANSP minus PD_EQ). Precipitation rates are decreased over mountains and high elevations and no significant change can be seen over Asia. Adding the vegetation model and a land surface scheme increases the precipitation rates over the continents dramatically (Fig. 4b, PD_LV minus PD_M_TRANSP). South America, South Africa, northern Australia and southeast Asia experience higher precipitation rates due to the local hydrological cycle induced by the existence of plants and evapo-transpiration. Northern Asia shows an increase of up to 0.6 m/year due to the presence of vegetation. Finally, Fig. 4c (PD_LV minus PD_EQ) represents the combined effects of the new moisture transport parametrization and the presence of a land surface scheme and vegetation model. While the new parametrization for moisture transport is vital for the vegetation model to simulate a realistic vegetation cover, it is paramount that precipitation changes over land are mostly due to the presence of vegetation, not due to the new parametrization of moisture transport.

Comparing the precipitation rates of the uncoupled model (PD_EQ) and the model with vegetation

(PD_LV) with observations (Kalnay et al. 1996), we can conclude that the introduction of land surface feedbacks highly improves the simulated precipitation field over land (see Fig. 5b). Precipitation rates over northern Asia, North America, South America and Africa are increased in comparison to the model without the vegetation model (PD_EQ run, Fig. 5a) and the patterns are in better agreement with observations (Fig. 5c).

Overall, the PD_LV control run shows good agreement with observations, especially on the zonal mean (Fig. 6). The global temperature is 0.61 °C warmer than observations, partly due to the fact that aerosols are not taken into account during this simulation and that the simulated air temperature corresponds to the present day atmospheric CO₂ concentration of 365 ppm whereas the NCEP data is a long term mean over the last decades. This discrepancy might be one of the causes for an enhanced hydrological cycle in the model leading to a globally averaged precipitation of 0.28 m per year higher than in the NCEP climatology.

The meridional overturning strength in the North Atlantic amounts to 20 Sv in our PD_LV control run, which is consistent with observed values of the present day overturning (Schmitz and McCartney 1993). About 12 Sv of NADW is transported across the equator into the South Atlantic (Fig. 7). Antarctic Bottom Water (AABW) is formed in the Ross and Weddell Seas and extends to about 40°N, filling the deep North Atlantic up to a depth of about 3000 m.

In summary, the PD_LV control run shows that the UVic ESCM with its two new components, a land surface scheme and a vegetation model, provides a reasonable simulation of the current climate. Some shortcomings which existed in the standard version of this model (Weaver et al. 2001) are still present in this new configuration (i.e. temperature anomalies over land masses and over the North Atlantic). Others, like the annually averaged precipitation field over land, have been improved. Agreement of the simulated vegetation cover with observations is comparable to other simulations obtained with an AOGCM coupled to TRIFFID. We conclude that the ESCM can serve as a useful tool to investigate the importance of climate processes in past, present and future climate simulations.

4 Ice age inception

To study vegetation related feedbacks during ice age inceptions, we integrate the coupled system under 116 ka BP conditions, with an atmospheric CO₂ concentration equal to 240 ppm (Schlesinger and Verbitsky 1996) and orbital parameters corresponding to 116 ka BP (Berger 1978). As the atmospheric model consists of an energy and moisture balance model, atmospheric dynamics are poorly represented. In this simulation, we compute surface pressure anomalies as a function of surface temperature anomalies. Wind and wind stress anomalies are then calculated (see Weaver et al. 2001 for

Fig. 4 Annually averaged precipitation in m/year, **a** effects of the new parametrization of moisture transport (PD_M_TRANSP minus PD_EQ), **b** effects of vegetation and land surface scheme (PD_LV minus PD_M_TRANSP), **c** combined effects of the new parametrization of moisture transport and vegetation/land surface scheme (PD_LV minus PD_EQ)

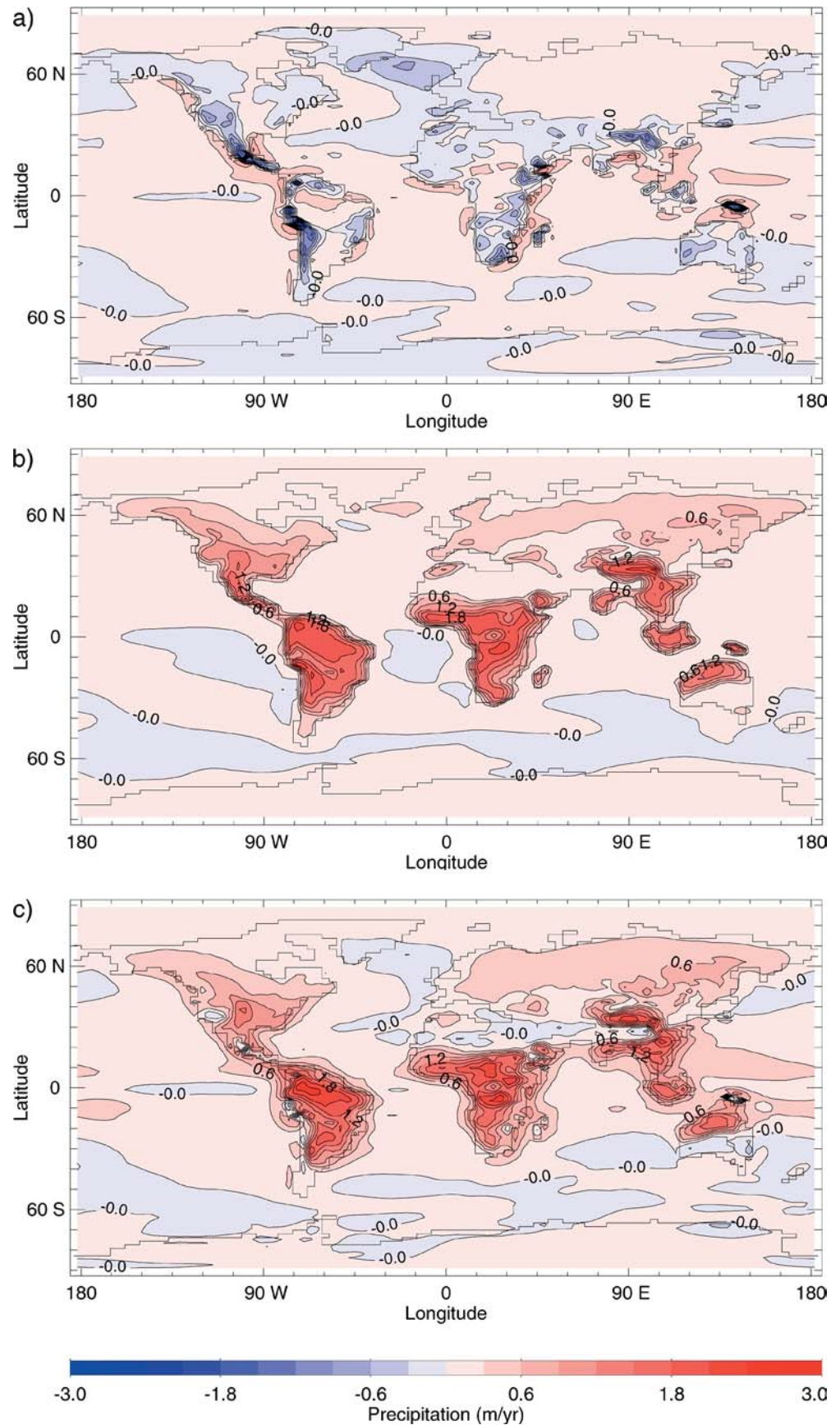


Fig. 5 Annually averaged precipitation in m/year from **a** model without vegetation and surface scheme (PD_EQ), **b** model as described in this study (PD_LV) and **c** NCEP climatology

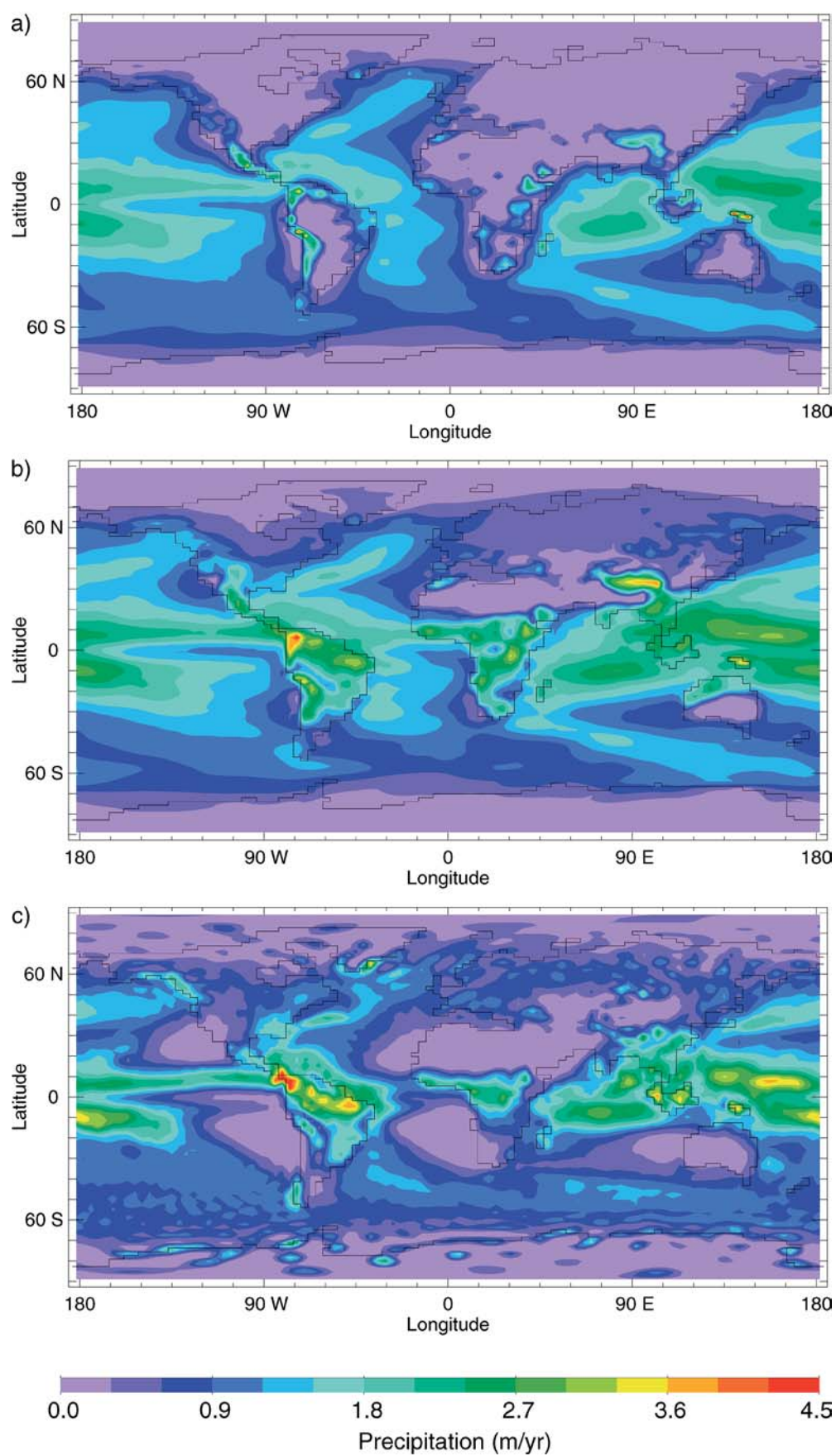
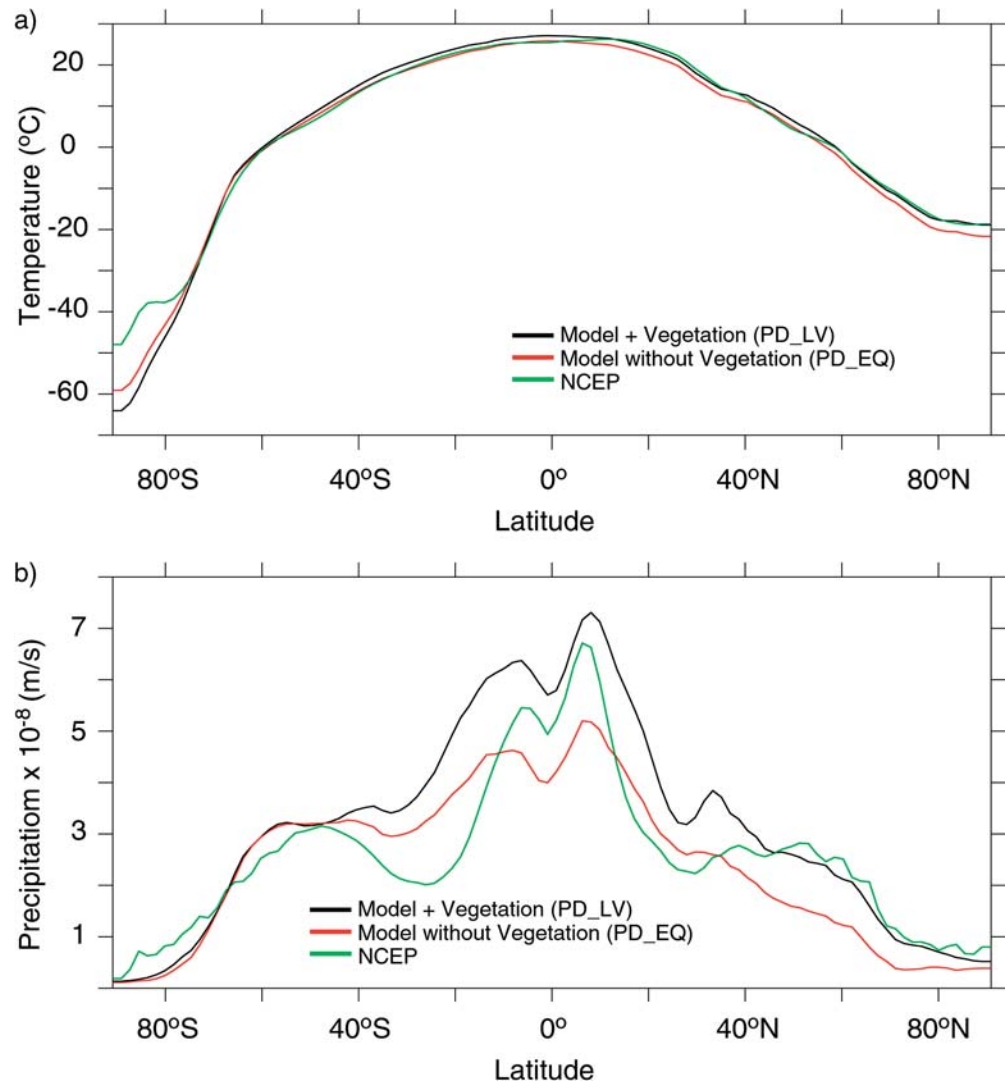


Fig. 6 Annually and zonally averaged **a** temperature and **b** precipitation. Simulations using the model without vegetation and surface scheme are represented in *red* (PD_EQ), results from the model as described in this study are in *black* (PD_LV) and NCEP data in *green*



a detailed description) and are added as a perturbation to the present day climatological wind fields. This ice age inception simulation with the coupled vegetation model and land surface scheme will be called 116 ka BP_LV hereafter.

The PD_LV control run (described in Sect. 3) includes anthropogenic land cover changes and an atmospheric CO_2 concentration due to human activity; it is therefore not suitable as a reference run in order to study differences between the climate system at 116 ka BP and the Holocene. Therefore, we use an equilibrium run under preindustrial conditions with atmospheric $[\text{CO}_2] = 280$ ppm, today's orbital parameters and no anthropogenic land cover changes (called PI_LV run) for comparison with the ice age inception run.

The total amount of vegetation carbon is reduced by 148 GtC (116 ka BP_LV versus PI_LV run) – a reduction of 20%, whereas the NPP is remarkably similar (decreases by only 2 GtC per year, corresponding to a 3% reduction). GPP is decreased by 13 GtC per year (9%) and the total amount of soil carbon stays almost unchanged (increases by 27 Gt or 3%). A possible

explanation for these global numbers is the fact that reduced atmospheric CO_2 concentrations and cooler temperatures tend to lower photosynthesis and thus GPP. On the other hand, lower temperatures also reduce plant respiration rates (20 Gt per year or 23%) which results in an almost unchanged rate of NPP. Table 2 gives a summary of carbon reservoirs and carbon fluxes from all the simulations described in this paper.

To assess the influence of vegetation related feedbacks during ice age inceptions, we also conducted two simulations with the standard UVic Earth System Model without the land surface scheme and vegetation model. Run PI and run 116 ka BP are forced with orbital parameters and atmospheric CO_2 concentrations as in the vegetation model runs (see Table 1 for an overview).

4.1 Ocean circulation changes

Figure 8 shows the meridional overturning in the Atlantic Ocean for PI_LV (Fig. 8a) and PI (Fig. 8b).

Fig. 7 Annually averaged overturning motion in the North Atlantic (in Sv, PD_LV simulation)

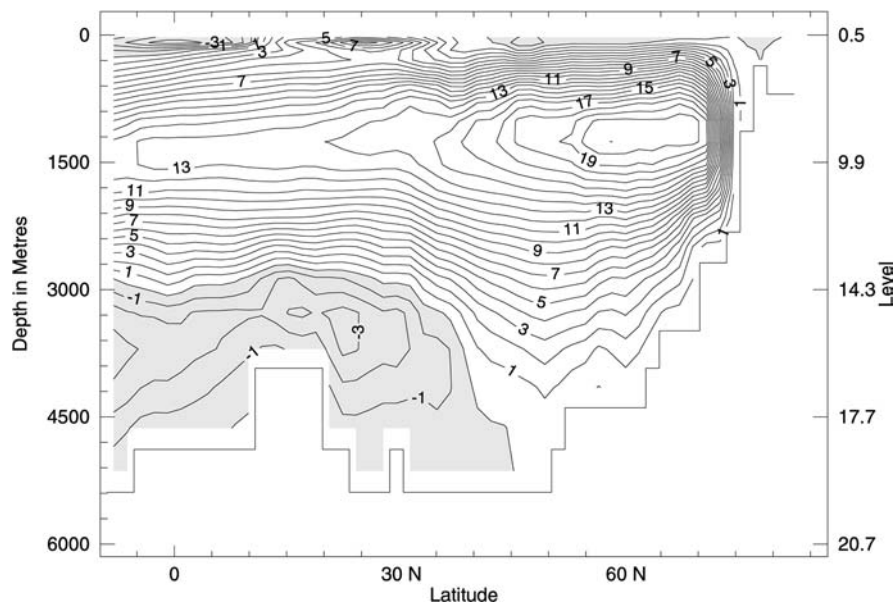


Table 2 Global values of carbon fluxes (in GtC/year) and carbon reservoirs (in GtC)

Simulation	NPP	GPP	vegetation Carbon	Soil Carbon	Soil respiration
PD_EQ_LV	81	187	887	1117	82
PD_LV	83	184	752	1104	82
PI_LV	61	148	753	946	62
116 ka BP_LV	59	135	605	973	59
PI_240_LV	60	138	572	919	61

The patterns are very similar: the maximum overturning reaches 21 Sv and 23 Sv in PI_LV and PI respectively. AABW fills the deep North Atlantic up to a depth of about 3000 m and expands north to about 35°N. AABW formation is slightly enhanced in the PI_LV simulation compared to the PI run, while NADW formation is slightly reduced (deep water formation see-saw Stocker 2000). Comparing Fig. 8c and d (116 ka BP_LV versus 116 ka BP), the conclusions are very similar: 116 ka BP simulates higher NADW and lower AABW formation than 116 ka BP_LV. The difference between ice age inception runs and preindustrial control runs are shown in Fig. 8e (model with vegetation) and Fig. 8f (model without vegetation). While the uncoupled standard model (without vegetation) only experiences a reduction of 1.9 Sverdrup, the weakening of the meridional overturning in the North Atlantic is more pronounced when vegetation related feedbacks are included. About 3 Sv less NADW is transported over the Equator into the Southern Hemisphere, and the maximum is reduced by 3.8 Sv. These circulation changes have an impact on the meridional heat transport in the oceans. As can be seen in Fig. 9, the global oceanic northward heat transport is reduced by up to 0.15 Peta Watt when comparing 116 ka BP_LV to

PI_LV. Thus vegetation related feedbacks double the effect induced by changes in orbital parameters and atmospheric CO₂ on the behavior of the thermohaline circulation. These findings are different from transient simulations carried out with ‘MoBiDic’ (Crucifix and Loutre 2002). Only a slight change in the strength of the thermohaline circulation (5% weakening) has been found by Crucifix and Loutre (2002) without any significant impact on the heat balance of the northern high latitudes between 126 and 115 ka BP.

The reduction of the meridional circulation during ice age inception is due to two different physical mechanisms. First the reduced CO₂ partial pressure leads to a reduction of radiative forcing and thus to a global cooling. As sea water density is more sensitive to temperature changes in low than in high latitudes, a global decrease in temperature results in a decrease in the meridional density gradient and thus in a weakening of the meridional overturning in the North Atlantic (Hughes and Weaver 1994). Second, the orbital configuration at 116 ka BP is characterized by a larger eccentricity and a smaller obliquity than today, reducing the seasonality in the Northern Hemisphere. Due to a higher annual snow cover, the cooling is strongest at high latitudes, leading to cooler SSTs and an increased sea ice cover in the North Atlantic (Fig. 10a, b). This effect is enhanced when vegetation dynamics are included due to the vegetation shift and associated albedo change (see Sect. 4.2). Sea ice inhibits deep water formation and the sea surface salinities (SSSs) are decreased in regions where the sea ice extent is changed (Fig. 10c, d), resulting in a decrease of deep water formation in the North Atlantic.

As the present study is one of the first glacial inception simulations done with an Earth System Model that includes an ocean GCM, it is also a useful tool to assess deep ocean temperature changes. These

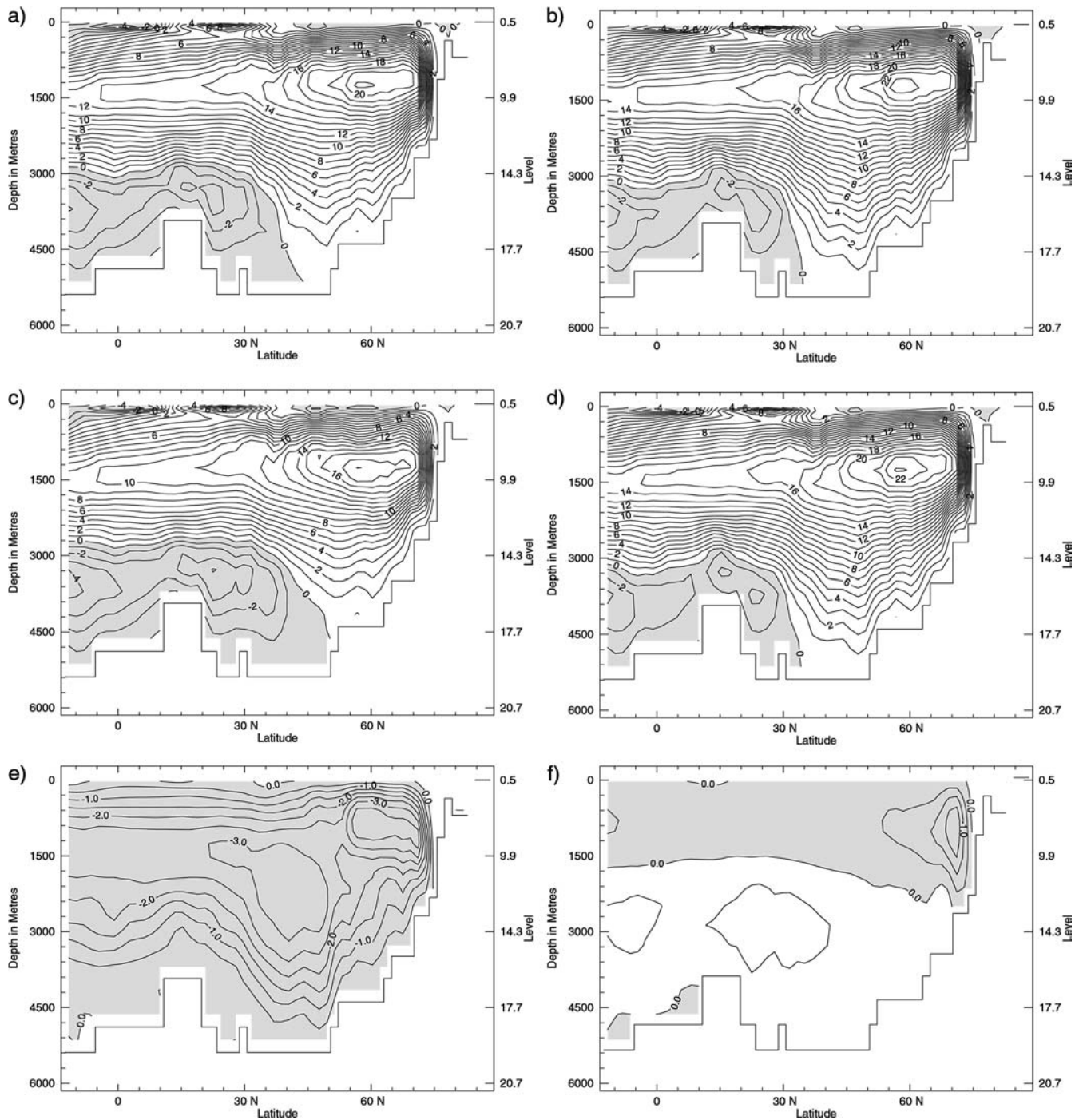


Fig. 8 Annually averaged overturning motion in the North Atlantic (in Sv) **a** simulation PI_LV, **b** simulation PI, **c** simulation 116 ka BP_LV, **d** simulation 116 ka BP, **e** difference between the 116 ka BP_LV simulation and the PI_LV control run, **f** difference between the 116 ka BP simulation and the PI control run

temperature changes are of interest in separating the temperature and ice volume effects when interpreting benthic $\delta^{18}\text{O}$ records. Figure 11 shows the difference of bottom water temperatures between the 116 ka BP_LV and the PI_LV simulation. The most important changes can be seen in the Arctic Basin, where bottom water temperatures are up to 3.5 °C colder during the

ice age inception simulation. Water characteristics also changed in the Atlantic Ocean: bottom water temperatures increased by up to 0.5 °C along the continental shelf and decreased by up to 0.5 °C in the deep basin in comparison with the preindustrial control run. These temperature changes reflect the change in NADW: deep water formation sites are situated fur-

Fig. 9 Annually averaged meridional heat transport in the ocean in Peta Watt: difference between 116 ka BP_LV and PI_LV (solid line) and 116 ka BP and PI (dashed line), positive numbers indicate a northward transport

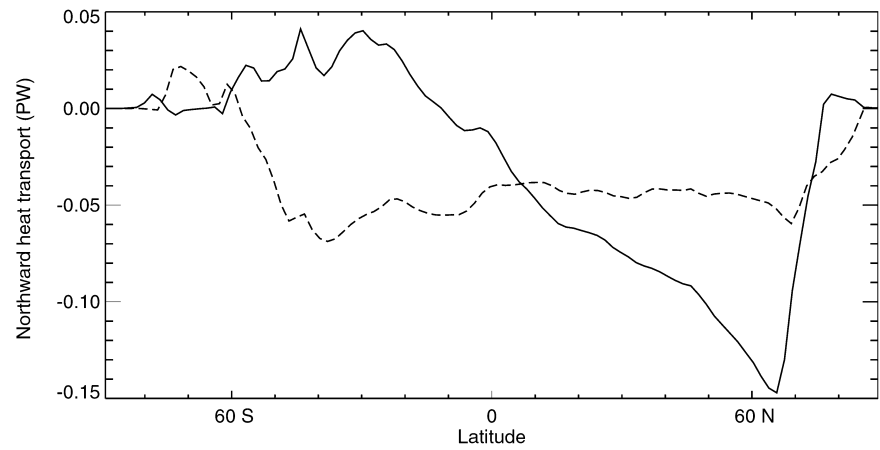
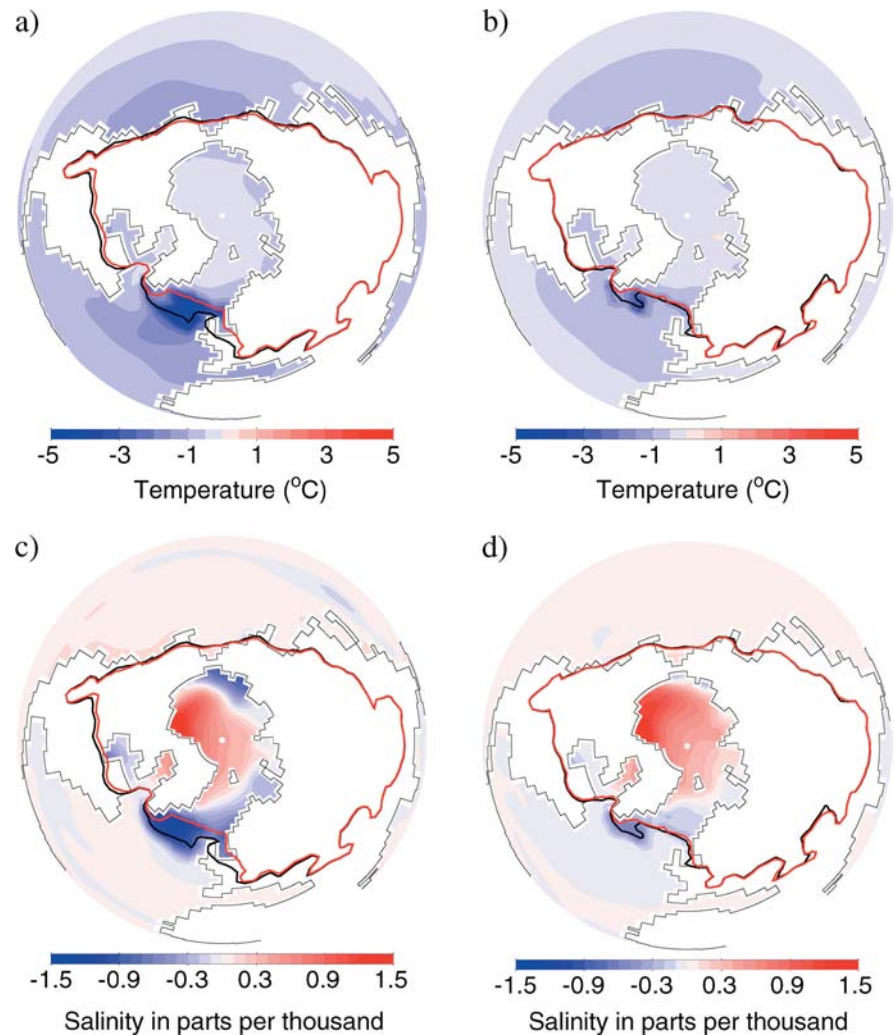


Fig. 10 Annually averaged sea surface temperatures **a** difference between the 116 ka BP_LV and PI_LV simulation; **b** difference between the 116 ka BP and PI simulation – and annually averaged sea surface salinities, **c** difference between the 116 ka BP_LV and PI_LV simulation; **d** difference between the 116 ka BP and PI simulation. The maximum ice edge is also represented (black line for the 116 ka BP runs and red line for the PI runs)



ther south during the ice age inception run and NADW is thus slightly warmer than during the control run, consistent with Meissner and Gerdes (2002). Apart from shallow coastal waters, the Indian and Pacific Ocean experience almost no bottom water temperature change.

4.2 High latitude vegetation changes and snow accumulation

With a globally colder climate, one would expect a southward migration of the treeline in high northern latitudes. The areal coverage of needleleaf trees is

Fig. 11 Annually averaged bottom temperatures in °C - difference between the 116 ka BP_LV and PI_LV simulation

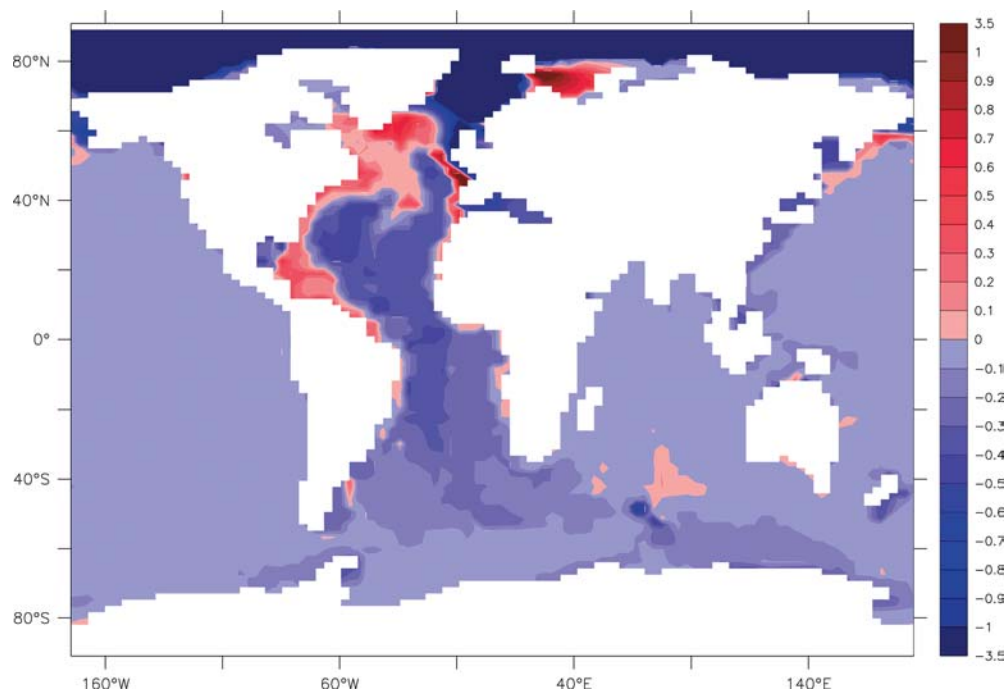
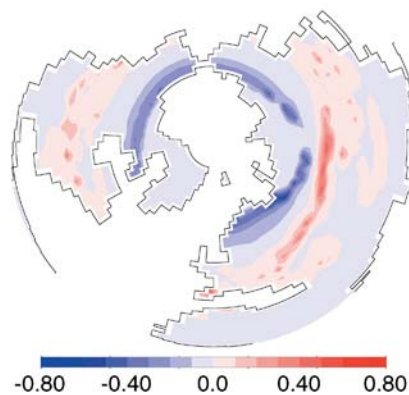
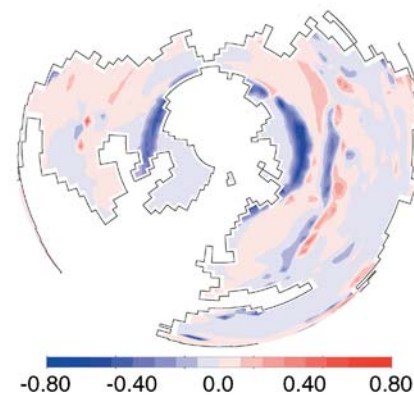


Fig. 12 Annually averaged areal coverage of **a** needleleaf trees, **b** shrubs, **c** C₃ grasses and **d** surface albedo - difference between the 116 ka BP_LV simulation and the PI_LV control run

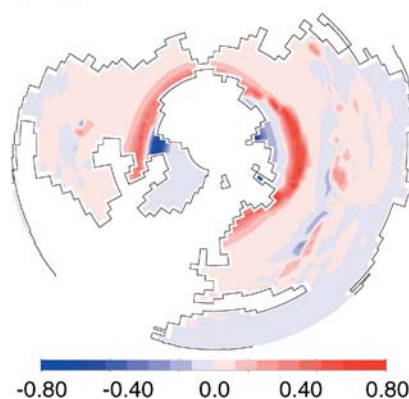
a) Needleleaf Trees



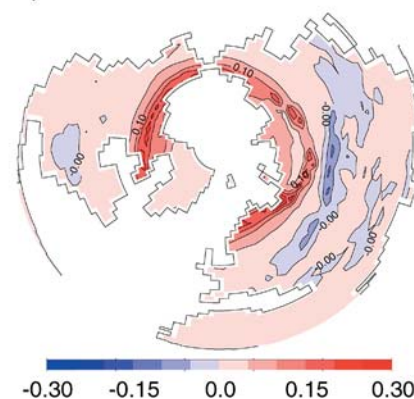
b) Shrubs



c) C₃ Grasses



d) Surface Albedo



effectively reduced by up to 50% in northern Europe, Asia and North America when comparing 116 ka BP_LV with PI_LV (see Fig. 12a). By the same token, up to 80% of the shrub cover disappeared in some regions of North America and Siberia (Fig. 12b). Needleleaf trees and shrubs were replaced by C_3 grasses in these regions (Fig. 12c). As the simulated albedo during winter months takes into account the snow masking effect of evergreen trees, this vegetation shift

leads to important differences in the annual mean local surface albedo, which increased by up to 0.26 in locations where needleleaf trees disappeared (see Fig. 12d). Vegetation changes in high latitudes amplify the cooling over the Northern Hemisphere as can be seen in Fig. 13 where differences in atmospheric surface temperature between the 116 ka BP_LV and PI_LV run are compared with the same patterns obtained by the climate model without vegetation (116 ka BP minus PI). The maximum of atmospheric temperature change is located over regions in the North Atlantic where the sea ice cover changed significantly between the 116 ka BP_LV and the PI_LV run (Fig. 10). Vegetation changes amplify the atmospheric cooling through albedo changes leading to enhanced sea ice formation, which in turn is responsible for the maximum cooling over eastern Greenland and the Irminger Sea as well as for part of the reduction of meridional overturning. Changes in land cover have thus an important influence on the ocean circulation as well as on the sea ice cover in northern high latitudes. The global cooling amounts to -0.9°C (116 ka BP_LV minus PI_LV) versus -0.5°C (116 ka BP minus PI).

The annual mean snow thickness is increased over large regions in North America, Siberia and Scandinavia. Perennial snow cover, considered as a minimum requirement for glacial inception, occurs over Canada and Siberia north of 60° – 70°N latitude. The vegetation and land surface model improved the simulated snow cover for the warmest month in the year under 116 ka BP conditions dramatically (see Fig. 14 for a comparison). Whereas perennial snow occurs only over Greenland, Spitzbergen and two small regions located near the Canadian Alaskan border in the simulation without the land-vegetation model, the effect of vegetation changes expands these regions to encompass the whole Arctic. Crucifix and Loutre (2002) come to similar conclusions with their simulation of an ice age inception by showing that the area of perennial snow north of 60°N increases significantly with increasing fraction of tundra and cold desert.

These findings are also consistent with Yoshimori et al. (2002) who investigated the response of an AGCM to changes in lower boundary conditions during ice age inception runs, and found that a realistic global net snow accumulation rate was only obtained when 116 ka BP sea surface conditions and modified land surface conditions were applied. Yoshimori et al. (2002) concluded that vegetation change has a large impact on climate during ice age inceptions. It is important to note, however, that the sensitivity of climate-vegetation models to changes in tree cover at high northern latitudes is highly model dependent. Brovkin et al. (2003) show that the Belgian model ‘MoBiDic’ shows stronger sensitivity to boreal deforestation than the German model ‘CLIMBER-2’. Comparing ice age inception runs, vegetation related feedbacks are more important for ‘MoBiDic’ than for ‘CLIMBER-2’ (Victor Brovkin personal communication).

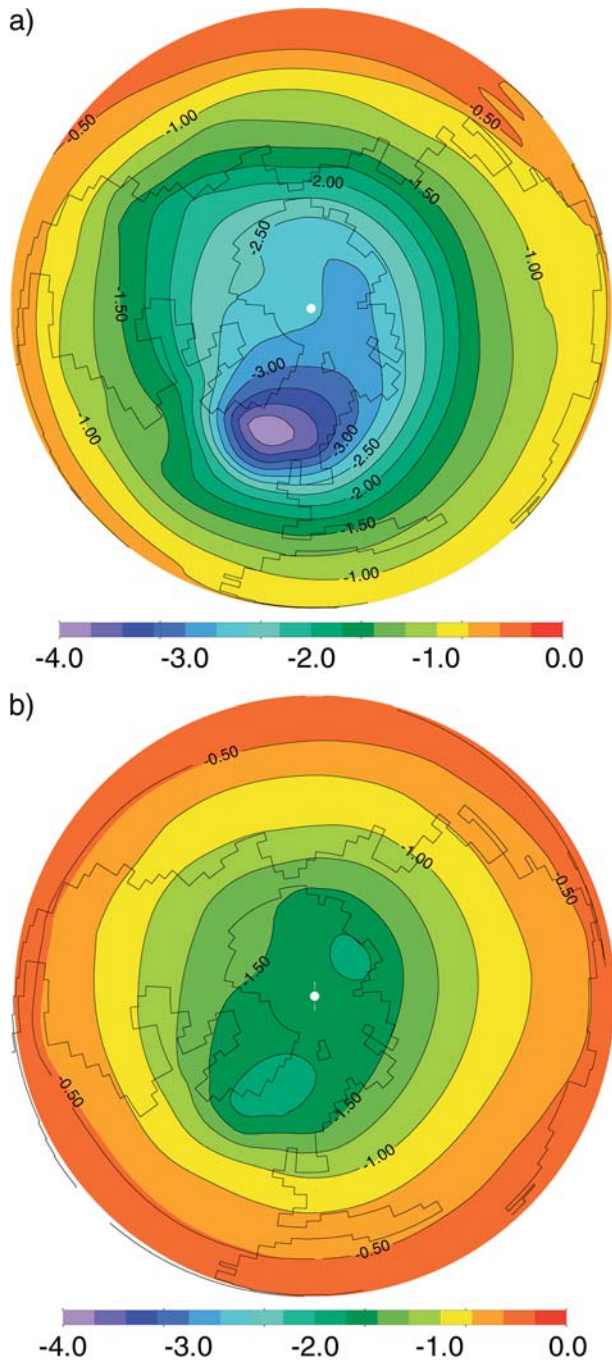


Fig. 13 Annually averaged atmospheric temperature (in $^\circ\text{C}$) **a** difference between the 116 ka BP_LV and the PI_LV simulation and **b** difference between the 116 ka BP and the PI simulation

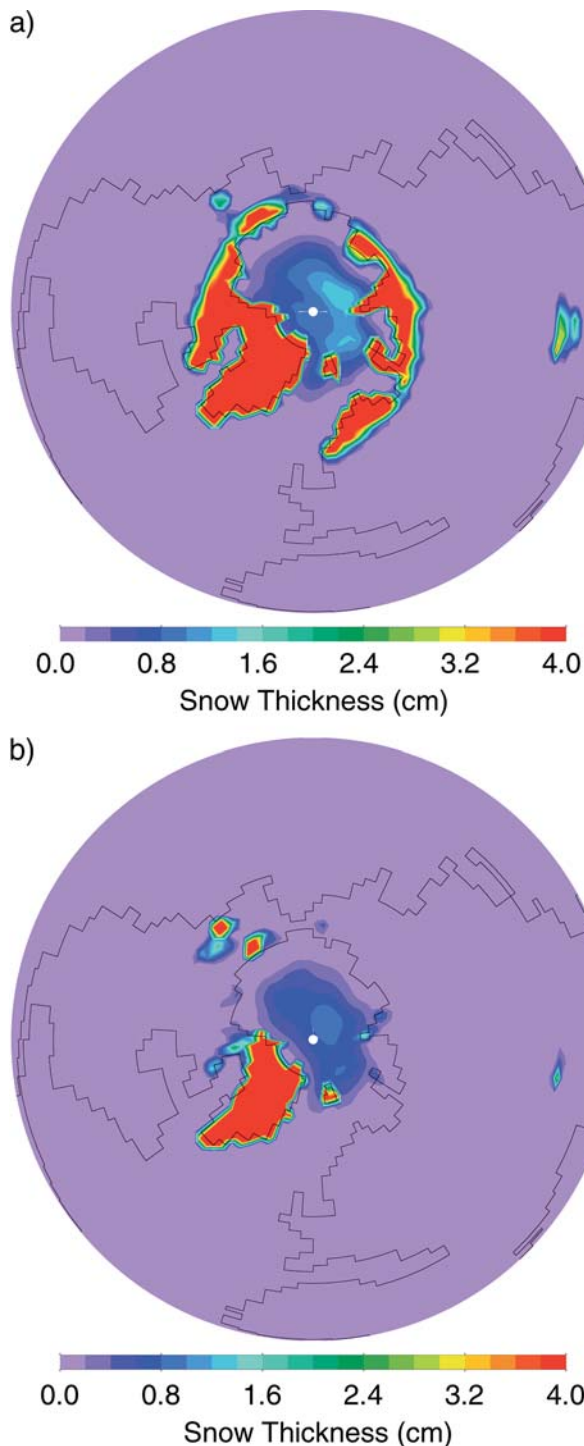


Fig. 14 Monthly averaged lying snow (in cm) for September – 116 ka BP_LV simulation with **a** the fully coupled model and **b** the climate model without vegetation and land surface scheme (116 ka BP simulation). All locations where the snow thickness exceeds 4 cm are colored in red

The global snow accumulation rate in simulation 116 ka BP_LV amounts to $3.74 \cdot 10^{12}$ kg per year, where the global snowfall, global melting and global sublimation rates are $1.456 \cdot 10^{16}$ kg/year, $3.544 \cdot 10^{15}$ kg/year and $1.101 \cdot 10^{16}$ kg/year respectively. Considering

this snow accumulation rate as constant over 10,000 years, the net contribution to continental ice sheets over 10,000 years amounts to $3.74 \cdot 10^{13}$ m³ (corresponding to 0.1 m of sea level change) which is considerably less than estimates derived from sea level records. It should be kept in mind, however, that continental ice sheets introduce a positive feedback to the system by lowering the temperature locally due to higher topography and higher albedo. Considering a constant snow accumulation rate over 10,000 years leads therefore to an underestimation relative to a case where ice sheets start to grow.

Figure 15a shows the amount of precipitation falling as snow in the 116 ka BP_LV simulation. The highest snowfall rates can be found over western North America, the Himalayas, Scandinavia and eastern Asia. The model simulates a very low snowfall rate over the nucleation sites of the Laurentide icesheet. In comparison to the PI_LV run, snowfall rates increased over western North America, western Europe and the Himalayas (Fig. 15b). The global snowfall rates are highest during the boreal winter months (Fig. 16), global sublimation rates follow the snowfall rate with a timelag of about 2 months and global melting rates are highest during the boreal spring and early summer. In comparison to the PI_LV simulation, snowfall is increased during the boreal summer, whereas sublimation rates are increased during late summer and fall and melting rates are decreased in early summer and increased during late summer (Fig. 16).

4.3 Changes in tropical regions

An additional feature of the initial ice growth interval involves tropical aridity (Crowley and North 1991). For example, Stokes et al. (1997) report several arid events in the Kalahari desert since the last interglacial period, one of which is dated ~ 115 –95 ka BP and corresponds to a dune-building (arid) phase. However, there are only a few paleo datasets for vegetation changes covering the last interglacial and ice age inception. Most of them come from Europe or South America, often with a time scale dependent on the marine stratigraphy (Guiot 1997). The long European records are in regions where it is often difficult to separate the vegetation response to climate from the response to ecological controls (Whitlock and Bartlein 1997). An interesting study has been carried out by Bird and Cali (1998) who analyzed a deep sea sediment core on the Sierra Leone Rise to infer a million-year record of fire in sub-Saharan Africa. Low fire incidence implies wet conditions and extensive C₃-dominated forests. An increased fire incidence means the expansion of savannas in drier conditions and an increased proportion of C₄ grasses in the biomass being burnt. Bird and Cali (1998) conclude that intense episodes of vegetation fires occurred during periods when global climate was changing from an interglacial to a glacial mode.

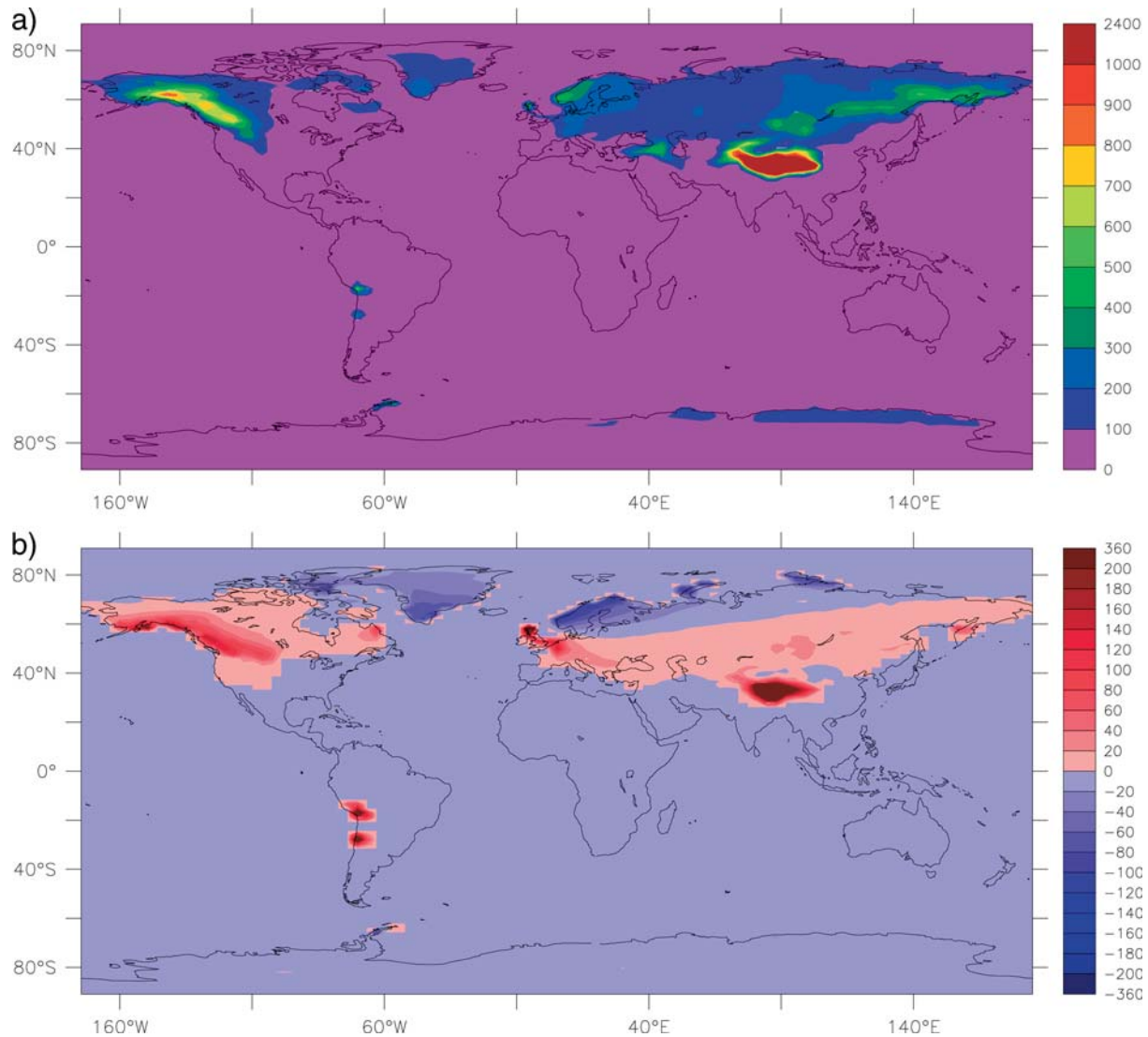


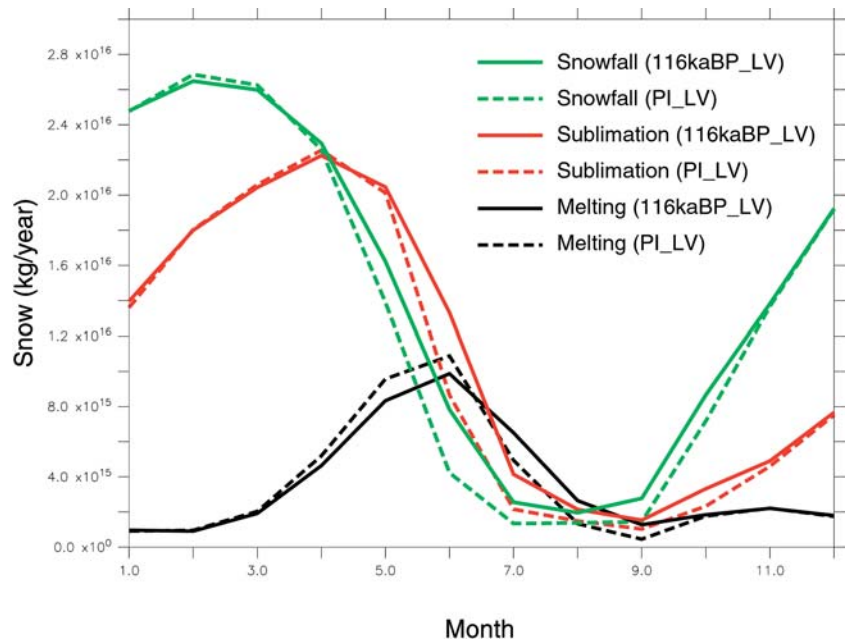
Fig. 15 Annually averaged snowfall rate (in kg/(m² year)) **a** 116 ka BP_LV simulation and **b** difference between 116 ka BP_LV and PI_LV

Model results from the present study show a shift in tropical vegetation during the last ice age inception (Fig. 17). The areal coverage of broadleaf trees is reduced by up to 40% in the sub-Saharan in comparison with the preindustrial LV run; these differences are enhanced in eastern South America, South Africa and in southeastern Asia. In our simulation, most of the C₃-dominated tropical forests have been replaced by shrubs (Fig. 17b) and to a lesser extent by C₄ grasses. The soil moisture in eastern South America and South Africa is reduced by up to 125 kg/m² (corresponding to a 50% decrease) in comparison with the preindustrial LV run, whereas southwestern Australia is characterized by wetter conditions, leading to a partial ‘greening’ of the desert in the form of C₄ grasses and shrubs (Fig. 18). The drier conditions in Amazonia, the Brazilian Highlands and South Africa are responsible for most of the vegetation shifts in these regions. However, in the sub-Saharan and in southeastern Asia, differences in the

precipitation and soil moisture fields are negligible. The physiological response of photosynthesizing plants to lower atmospheric CO₂ concentrations is the main cause for vegetation changes in these regions.

To assess the impact of a reduced atmospheric CO₂ concentration on the vegetation, we ran a sensitivity study under preindustrial forcing (insolation, CO₂ and wind fields) where only the vegetation model ‘sees’ an atmospheric CO₂ concentration corresponding to 116 ka BP conditions (run PI_240_LV). Fig. 19 shows the vegetation changes due to the physiological response of plants to lower CO₂ concentrations (difference between black and green line) and those due to climate change (difference between red and green line). The low atmospheric CO₂ concentrations account for a large part of the observed vegetation shift north of 10°S (green and red line follow each other closely). Between 10°S and 30°S (comprising Amazonia, the Brazilian Highlands and South Africa), vegetation shifts are due to both

Fig. 16 Annual cycle of globally averaged snowfall rate (green), sublimation (red) and melting (black) for the 116 ka BP_LV simulation (solid lines) and the PI_LV simulation (dashed lines). All values are in $\text{kg}/(\text{m}^2 \text{ year})$ and the x -axis indicates the month (1 = January, etc.)



changes in climate and lower CO_2 concentrations. It is interesting to note that in some regions (around 35°N for example) climate change offsets partly the changes due to CO_2 concentration change (red line located between black and green line).

5 Conclusions

Two new components of the UVic Earth System Model, a land surface scheme and a vegetation model, have been introduced in the present study. The five model components (ocean, sea ice, atmosphere, land surface and vegetation) are coupled without any flux adjustments: freshwater and energy are conserved to machine precision. A present day control run shows that the introduction of land related processes improved the precipitation field over continents. Precipitation rates over northern Asia as well as North and South America are significantly higher and their patterns are in better agreement with observations than in simulations without the vegetation and land surface models included. The simulated present day vegetation is in good agreement with observations whereas the atmospheric temperature as well as the ocean state and circulation have only been slightly affected by the introduction of land model components. As the incoming solar radiation, wind fields and atmospheric CO_2 concentration are the only 'external' data driving the model, it is well suited to investigate scenarios which deviate from present conditions.

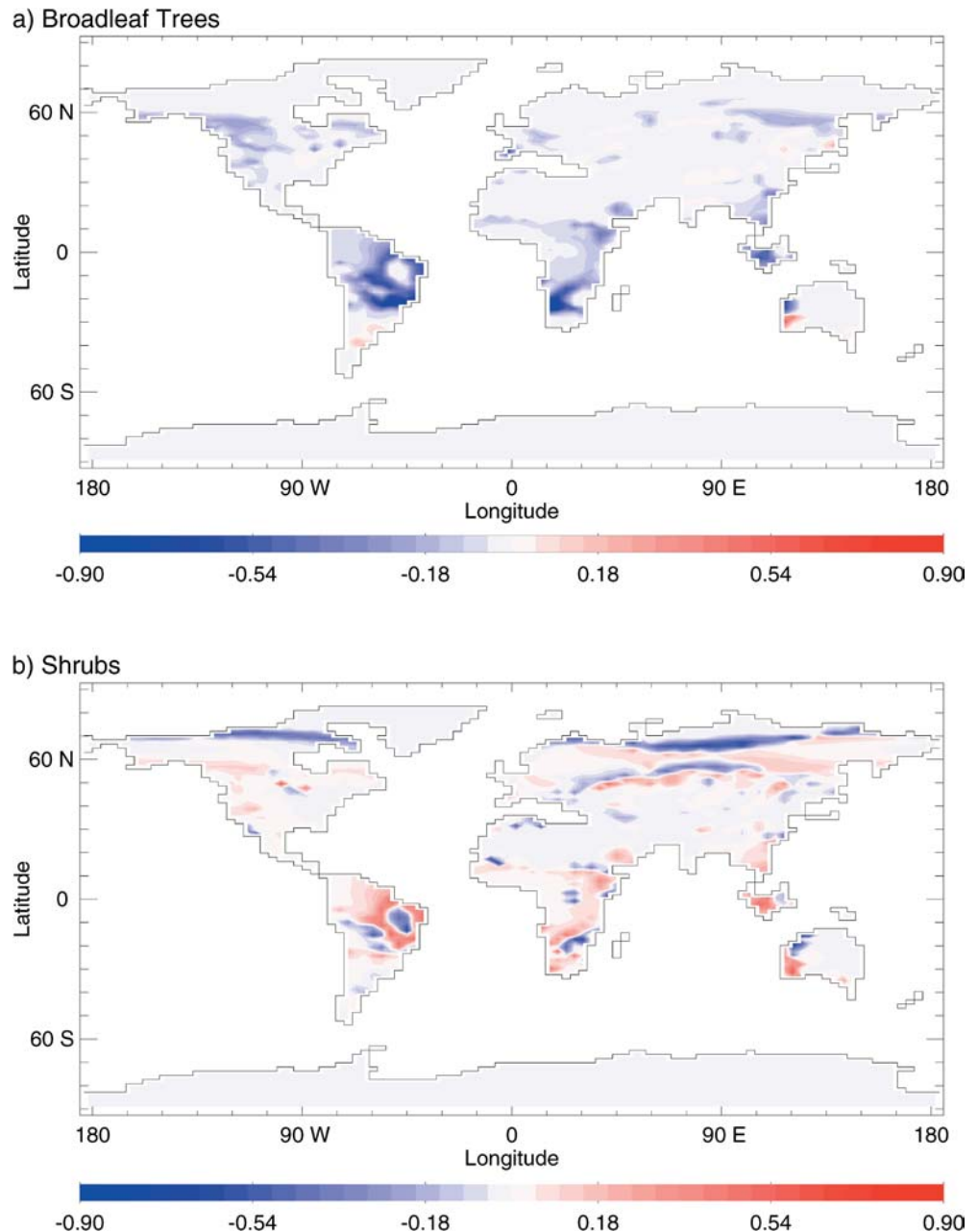
An ice age inception simulation forced by reduced atmospheric CO_2 levels and orbital parameters corresponding to 116 ka BP shows a southward shift of the northern treeline as well as a global decrease in vegetation carbon. At the same time, the oceanic meridional overturning in the North Atlantic is reduced by 3.8 Sv (versus 1.9 Sv in the standard model without vegetation and land

surface scheme). Atmospheric cooling occurs principally over the northern North Atlantic, suggesting that changes in the oceanic circulation and sea ice serve to further amplify the cooling forced by vegetation and surface albedo changes. A comparison with results from the standard UVic Earth System Model without vegetation and land surface components shows that vegetation changes increase areas with perennial snow significantly.

Another interesting feature of the ice age inception simulation is the fact that up to 88% of broadleaf trees are replaced by shrubs in tropical regions. This shift in vegetation is partly due to the reduced atmospheric CO_2 concentration. Over South America and South Africa large changes in precipitation and soil moisture also contribute to a decrease in the areal coverage of broadleaf trees. Concurrent with the drier conditions in South America and Africa, Australia experiences increased soil moisture leading to a greening of the Australian desert. It is difficult to assess these results due to a shortage of paleo vegetation data. More long sequences of pollen data, especially in the tropical monsoon regions would contribute to a better understanding of the influence of abrupt climate changes on vegetation.

The total amount of vegetation carbon as well as the gross primary productivity (GPP) decreases with decreasing atmospheric CO_2 concentrations (see Table 2). Between the 116 ka BP_LV run and the PI_LV control run, vegetation carbon and GPP are reduced by 20% and 9% respectively. The PD_LV run simulates less vegetation carbon than the PI_LV control run: this is due to anthropogenic land cover changes, trees are replaced by grasses in large regions in the North American, European and Asian cereal belts. The soil carbon reservoir is almost steady (3% increase between PI_LV and 116 ka BP_LV runs). Soil respiration and soil carbon are significantly higher for the two present day simulations compared with the three other runs.

Fig. 17 Annually averaged areal coverage of **a** broadleaf trees and **b** shrubs - difference between the 116 ka BP_LV simulation and the PI_LV control run



Our results reaffirm the importance of vegetation feedbacks in glacial inception. When combined with cooler sea surface temperatures and a more southward sea ice extent associated with a slightly reduced North Atlantic overturning, the resulting feedbacks to Milankovitch forcing are sufficient to cause significant cooling in the Northern Hemisphere and large areas with permanent snow cover. A challenge that remains is to see whether the incorporation of a dynamic ice sheet model would allow continental glaciers to grow in these regions of snow accumulation.

Acknowledgements The authors would like to thank Michael Eby and Ed Wiebe for their technical support. Victor Brovkin, Michel Crucifix and one anonymous reviewer were extraordinarily

helpful with an earlier version of this paper. We are grateful for research grant support under the NSERC Operating, CSHD and CFCAS research grant programs. Andrew J. Weaver is grateful for release time provided by the Killam Fellowship and Canada Research Chair Programs. Peter M. Cox was supported by the UK Department of Environment, Food and Regional Affairs under The Climate Prediction Programme contract PECD 7/12/37.

Appendix 1: Land Surface Scheme

The land surface scheme consists of a simplified version of 'MOSES' (Met Office Surface Exchange Scheme) described in Cox et al. (1999a). The scheme used here defines the state of the land surface in terms of lying snow, skin temperature, soil temperature and

Fig. 18 Annually averaged changes in soil moisture in percent between the 116 ka BP_LV simulation and the PI_LV control run. Areas where soil moisture increased by more than 100% are colored in red

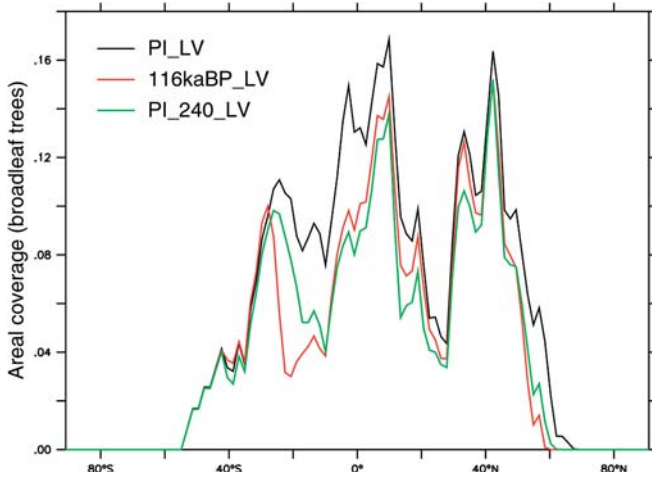
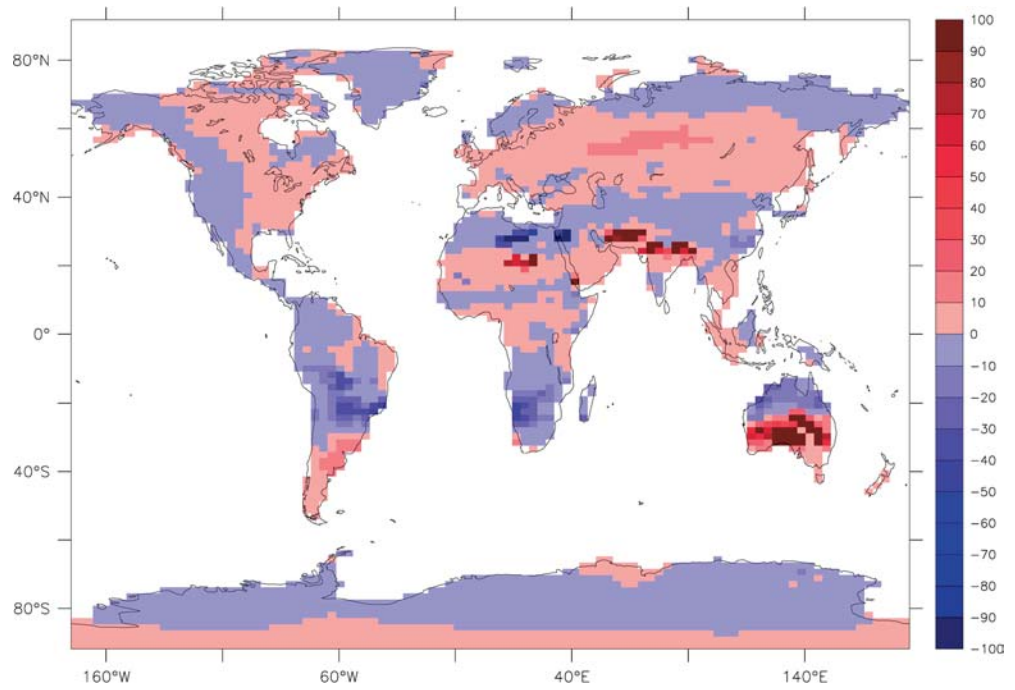


Fig. 19 Annually and zonally averaged coverage of broadleaf trees for the PI_LV run (black), 116 ka BP_LV run (red) and a preindustrial run where the vegetation only is forced with 116 ka BP atmospheric CO₂ concentrations (PI_240_LV, green)

Table 3 Constant parameters of the land surface scheme

Parameter	Description	Value
P^*	Atmospheric surface pressure	10^5 Pa
R	Gas constant	$287.05 \text{ J kg}^{-1} \text{ K}^{-1}$
K_S	Saturated hydraulic conductivity	$0.0047 \text{ kg m}^{-2} \text{ s}^{-1}$
b	Clapp-Hornberger exponent	6.6
L_c	Latent heat of condensation	$2.501 \cdot 10^6 \text{ J kg}^{-1}$
L_f	Latent heat of fusion	$0.334 \cdot 10^6 \text{ J kg}^{-1}$
σ	Stefan Boltzmann constant	$5.67 \cdot 10^{-8} \text{ W m}^{-2} \text{ K}^{-4}$
c_p	Specific heat capacity of dry air	$1005 \text{ J kg}^{-1} \text{ K}^{-1}$
λ	Soil heat conductivity	$0.23 \text{ W m}^{-1} \text{ K}^{-1}$
Δz_1	Thickness of the soil layer	1 m
C_S	Soil heat capacity	$3.3 \cdot 10^5 \text{ W m}^{-3} \text{ K}^{-1}$
M_{SAT}	Saturated soil moisture	458 kg m^{-2}
Θ_w	Wilting soil moisture	$0.136 \text{ m}^3(\text{H}_2\text{O})/\text{m}^3$ (soil)
Θ_c	Critical soil moisture	$0.242 \text{ m}^3(\text{H}_2\text{O})/\text{m}^3$ (soil)

moisture content, using a single soil layer. It recognizes the five TRIFFID vegetation types as well as bare soil (see Table 3 for values of constant parameters).

Soil moisture and snow mass

The soil moisture is updated according to:

$$\frac{\partial M}{\partial t} = P_R + S_M - E_M - Y \quad (1)$$

where M is the soil moisture in the top 1 m of soil, P_R the precipitation rate (rain), S_M the snow melt, E_M the evaporation rate and Y the continental runoff. The evaporation rate E_M is made up of transpiration by vegetation E_v and bare soil evaporation E_b

($E_M = E_v + E_b$). Transpiration by vegetation E_v is calculated separately for each plant functional type (PFT) i ($E_v = \sum E_{v,i}$) and occurs from the vegetated fraction v ($v = \sum v_i$):

$$E_{v,i} = v_i \frac{\rho}{r_a + r_{c,i}} (q_{sat}(T_i^*) - q_1) \quad (2)$$

where ρ is the surface air density, r_a the aerodynamic resistance (depending on roughness length and windspeed), $r_{c,i}$ the canopy resistance of PFT i , $q_{sat}(T_i^*)$ the saturated specific humidity at the skin temperature T_i^* and q_1 the atmospheric specific humidity (Cox et al. 1999a). The surface air density ρ is calculated with the constant surface pressure P^* and the surface air temperature T_1 ($\rho = P^*/(RT_1)$). The canopy resistance r_c is the inverse of the canopy conductance, g_c , which is calculated within the canopy conductance and primary productivity module described in Cox et al. (1999a). Bare soil evaporation E_b is defined as follows:

$$E_b = (1 - v) \frac{\rho}{r_a + r_{ss}} (q_{sat}(T_b^*) - q_1) \quad (3)$$

where T_b^* is the bare soil skin temperature and r_{ss} is the soil surface resistance scaling inversely with the soil moisture availability factor $\mu(\Theta)$:

$$r_{ss} = \min \left(10^6, \frac{100}{\mu} \right) \text{sm}^{-1} \quad (4)$$

$$\mu(\Theta) = \begin{cases} 1 : & \Theta > \Theta_c \\ \frac{\Theta - \Theta_w}{\Theta_c - \Theta_w} : & \Theta_w < \Theta \leq \Theta_c \\ 0 : & \Theta \leq \Theta_w \end{cases} \quad (5)$$

Θ_w is the volumetric soil moisture concentration below which stomata close, Θ_c is the volumetric soil moisture concentration above which stomata are not sensitive to soil water and Θ the volumetric soil moisture. Finally, the runoff Y is given by:

$$Y = K_s \left(\frac{M}{M_{SAT}} \right)^{(2b+3)} \quad (6)$$

where K_s is the saturated hydraulic conductivity, M_{SAT} is the saturated soil moisture and b is the Clapp-Hornberger exponent. River drainage basins are described in Weaver et al. (2001). The snow mass is updated according to:

$$\frac{\partial S}{\partial t} = P_S - S_M - E_S \quad (7)$$

where S is the snow mass, P_S the rate of precipitation (snow), and E_S the rate of sublimation. The evaporative demand E is met by any lying snow first ($E = E_S$ if there is lying snow in the grid cell, $E = E_M$ otherwise).

Energy balance

The energy balance for each PFT and for bare soil (i indicates a PFT or bare soil) consists of the net radiation R_{N_i} , the latent heat due to evaporation or sublimation LE_i , the sensible heat H_i and the soil heat flux G_i :

$$R_{N_i} = LE_i + H_i + G_i \quad (8)$$

The net radiation is defined as follows:

$$R_{N_i} = R_{SW}^{down} (1 - \alpha_{s,i}) + R_{LW}^{down} - \sigma T_i^4 \quad (9)$$

where R_{SW}^{down} is the incoming short wave radiation at the surface, $\alpha_{s,i}$ is the surface albedo of PFT i , R_{LW}^{down} is the downward atmospheric longwave radiation and σ is the Stefan Boltzmann constant. The latent heat due to evaporation or sublimation LE_i can be written as:

$$LE_i = L_c E_{M,i} + (L_c + L_f) E_s \quad (10)$$

where L_c and L_f are the latent heat of condensation and fusion, respectively. The sensible heat is a function of the skin temperature T_i^* and the atmospheric temperature T_1 :

$$H = \frac{\rho c_p (T_i^* - T_1)}{r_a} \quad (11)$$

where c_p is the specific heat capacity of the air. Finally, the soil heat flux G_i is defined as follows:

$$G = \frac{2\lambda}{\Delta z_1} (T_i^* - T_S) \quad (12)$$

where λ is the soil conductivity, Δz_1 the thickness of the soil layer and T_S is the soil temperature. The soil temperature T_S is calculated as a function of the ground heat flux and the energy required to melt snow:

$$\frac{\partial T_S}{\partial t} = \frac{G}{C_S \Delta z_1} - L_f S_M \quad (13)$$

where C_S is the soil heat capacity. The surface energy balance Eq. (8) is solved using equations 9 to 12 to eliminate the skin surface temperature, which yields an extended Penman-Monteith equation for each surface type (Essery et al. (2003)).

Appendix 2: IGBP data set

In Sect. 3, the simulated vegetation cover is compared to the IGBP data set (Loveland and Belward 1997). The IGBP biomes have been converted to PFTs by Mike Dunderdale (see Dunderdale et al. 1999 for a detailed description on how this conversion has been carried out). As the photosynthetic pathways (C_3 versus C_4) are not distinguished in the IGBP dataset, the ratio has been estimated based on the ratio of “long grass” to “short grass” (Dunderdale et al. 1999; Wilson and Henderson-Sellers 1985).

To calculate the correlation between the areal coverage of simulated vegetation and IGBP data, the correlation for each PFT in each grid cell has been calculated as follows:

$$\text{corr}(\text{PFT}_i) = 1 - \frac{|\text{a real coverage}(\text{PFT}_i, \text{IGBP}) - \text{a real coverage}(\text{PFT}_i, \text{model})|}{2} \quad (14)$$

The total correlation represented in Fig. 2 is the minimum of each correlation in each grid cell:

$$\text{total_corr} = \min[\text{corr}(\text{PFT}_i)]_{i=1,5} \quad (15)$$

References

- Berger AL (1978) Long-term variations of daily insolation and quaternary climatic changes. *J Atmos Sci* 35: 2362–2367
- Betts AK, Ball JH (1997) Albedo over the boreal forest. *J Geophys Res* 35: 28,901–28,909
- Bird MI, Cali JA (1998) A million-year record of fire in sub-Saharan Africa. *Nature* 394: 767–769
- Bitz CM, Holland MM, Weaver AJ, Eby M (2001) Simulating the ice-thickness distribution in a coupled climate model. *J Geophys Res* 106: 2441–2464
- Broecker WS, Denton GH (1990) What drives glacial cycles? *Sci Am* 262: 48–56
- Brovkin V, Ganopolski A, Svirezhev Y (1997) A continuous climate-vegetation classification for use in climate-biosphere studies. *Ecol Modell* 101: 251–261
- Brovkin V, Levis S, Loutre MF, Crucifix M, Claussen M, Ganopolski A, Kubatzki C, Petoukhov V (2003) Stability analysis of the climate-vegetation system in the northern high latitudes. *Clim Change* 57: 119–138
- Clark PU, Clague JJ, Curry BB, Dreimanis A, Hicock SR, Miller GH, Berger GW, Eyles N, Lamothe M, Miller BB, Mott RJ, Oldale RN, Stea RR, Szabo JP, Thorleifson LH, Vincent JS (1993) Initiation and development of the Laurentide and Cordilleran ice sheets following the last interglaciation. *Quat Sci Rev* 12: 79–114
- CLIMAP Project Members (1981) Seasonal reconstructions of the earth's surface at the Last Glacial Maximum. *Geol Soc Am Map Chart Ser*, MC-36
- Collatz GJ, Ball JT, Grivet C, Berry JA (1991) Physiological and environmental regulation of stomatal conductance, photosynthesis and transpiration: a model that includes a laminar boundary layer. *Agri Forest Meteorol* 54: 107–136
- Collatz GJ, Ribas-Carbo M, Berry JA (1992) A coupled photosynthesis-stomatal conductance model for leaves of C_4 plants. *Aust J Plant Physiol* 19: 519–538
- Cox PM (2001) Description of the ‘TRIFFID’ dynamic global vegetation model. *Hadley Centre Technical Note* 24: 1–16

- Cox PM, Betts RA, Bunton CB, Essery RLH, Rowntree PR, Smith J (1999a) The impact of new land surface physics on the GCM simulation of climate and climate sensitivity. *Clim Dyn* 15: 183–203
- Cox PM, Huntingford C, Harding RJ (1999b) A canopy conductance and photosynthesis model for use in a GCM land surface scheme. *J Hydrol* 212–213: 79–94
- Cox PM, Betts RA, Jones CD, Spall SA, Totterdell IJ (2000) Acceleration of global warming due to carbon-cycle feedbacks in a coupled climate model. *Nature* 408: 184–187
- Crowley TJ, North GR (1991) *Paleoclimatology*. 18, Oxford Monographs On Geology And Geophysics, Oxford University Press, New York
- Crucifix M, Loutre MF (2002) Transient simulations over the last interglacial period (126–115 kyr BP): feedback and forcing analysis. *Clim Dyn* 19: 417–433
- de Noblet NI, Prentice IC, Joussaume S, Texier D, Botta A, Haxeltine A (1996) Possible role of atmosphere–biosphere interactions in triggering the last glaciation. *Geophys Res Lett* 23(22): 3191–3194
- Dong B, Valdes PJ (1995) Sensitivity studies of Northern Hemisphere glaciation using an atmospheric general circulation model. *J Clim* 8(10): 2471–2496
- Dunderdale M, Muller JP, Cox PM (1999) Sensitivity of the Hadley Centre climate model to different earth observation and cartographically derived land surface data-sets. The Contribution of POLDER and New Generation Spaceborne Sensors to Global Change Studies, Meribel, France, pp 1–6
- Essery RLH, Best MJ, Betts RA, Cox PM, Taylor CM (2003) Explicit representation of subgrid heterogeneity in a GCM land-surface scheme. *J Hydrometeorol* 4: 530–543
- Federer CA (1968) Spatial variation of net radiation, albedo and surface temperature of forests. *J Appl Meteorol* 7: 789–795
- Foley JA, Prentice IC, Ramankutty N, Levis S, Pollard D, Sitch S, Haxeltine A (1996) An integrated biosphere model of land surface processes, terrestrial carbon balance, and vegetation dynamics. *Global Biogeochem Cyc* 10(4): 603–628
- Friend AD, Shugart HH, Running SW (1993) A physiology-based model of forest dynamics. *Ecology* 74: 792–797
- Gallimore RG, Kutzbach JE (1995) Snow cover and sea ice sensitivity to generic changes in earth orbital parameters. *J Geophys Res* 100(D1): 1103–1120
- Gallimore RG, Kutzbach JE (1996) Role of orbitally induced changes in tundra area in the onset of glaciation. *Nature* 381: 503–505
- Guiot J (1997) Back at the last interglacial. *Nature* 388: 25–27
- Houghton JT, Ding Y, Griggs DJ, Noguer M, van der Linden PJ, Dai X, Maskell K, Johnson CA, eds (2001) *Climate change 2001: the scientific basis*. IPCC Third Assessment Report, Cambridge University Press, Cambridge, UK
- Hughes TMC, Weaver AJ (1994) Multiple equilibria of an asymmetric two-basin ocean model. *J Phys Oceanogr* 24: 619–637
- Kalnay E, Kanamitsu M, Kistler R, Collins W, Deaven D, Gandin L, Iredell M, Saha S, White G, Woollen J, Zhu Y, Chelliah M, Ebisuzaki W, Higgins W, Janowiak J, Mo KC, Ropelewski C, Wang J, Leetma A, Reynolds R, Jenne R, Joseph D (1996) The NCEP/NCAR 40-year reanalysis project. *Bull Am Meteorol Soc* 77(3): 437–471
- Loveland TR, Belward AS (1997) The IGBP-DIS global 1 km land cover data set, DISCover: first results. *Int J Rem Sens* 18(15): 3289–3295
- Marshall SJ, Clarke GKC (1999) Ice sheet inception: subgrid hypsometric parametrization of mass balance in an ice sheet model. *Clim Dyn* 15(7): 533–550
- Matthews HD, Weaver AJ, Eby M, Meissner KJ (2003) Radiative forcing of climate by historical land cover change. *Geophys Res Lett* 30(2): 1055
- Meehl GA, Washington WM (1990) CO₂ climate sensitivity and snow-sea-ice albedo parametrization in an atmospheric GCM coupled to a mixed layer ocean model. *Clim Change* 16: 283–306
- Meissner KJ, Gerdes R (2002) Coupled climate modelling of ocean circulation changes during ice age inception. *Clim Dyn* 18: 455–473
- Milankovitch M (1930) *Mathematische Klimalehre und astronomische Theorie der Klimaschwankungen*. Handbuch der Klimatologie. Gebrüder Bornträger, Berlin, Band 1, Teil A
- Mooney H, Roy J, Saugier B, eds (2001) *Terrestrial global productivity: past, present and future*. Academic Press, San Diego, USA
- Oglesby RJ (1990) Sensitivity of glaciation to initial snow cover, CO₂, snow albedo, and oceanic roughness in the NCAR CCM. *Clim Dyn* 4(4): 219–235
- Pacanowski RC (1995) MOM 2 documentation, user's guide and reference manual. Tech Rep 3, GFDL Ocean Group, Geophysical Fluid Dynamics Laboratory, Princeton, USA
- Phillipps PJ, Held IM (1994) The response to orbital perturbations in an atmospheric model coupled to a slab ocean. *J Clim* 7(5): 767–782
- Pollard D, Thompson SL (1997) Driving a high-resolution dynamic ice-sheet model with GCM climate: ice-sheet initiation at 116,000 BP. *Ann Glaciol* 25: 296–304
- Post WM, Pastor J (1996) LINKAGES – an individual-based forest ecosystem model. *Clim Change* 34: 253–261
- Prentice C, Farquhar GD, Fasham MJR, Goulden ML, Heimann M, Jaramillo VJ, Khesghi HS, Le Quere C, Scholes RJ, Wallace DWR (2001) *Climate change 2001: The Scientific Basis*. Contributions of Working Group I to the Third Assessment Report of the Intergovernmental Panel on Climate Change, chap. The carbon cycle and atmospheric carbon dioxide. Cambridge University Press, Cambridge, United Kingdom, pp 881
- Ramankutty N, Foley JA (1999) Estimating historical changes in land cover: croplands from 1700 to 1992. *Glob Biogeochem Cyc* 13: 997–1027
- Rind D, Peteet D, Kukla G (1989) Can Milankovitch orbital variations initiate the growth of ice sheets in a general circulation model? *J Geophys Res* 94(D10): 12,851–12,871
- Royer JF, Deque M (1983) Orbital forcing of the inception of the Laurentide ice sheet? *Nature* 304(5921): 43–46
- Royer JF, Deque M, Pestiaux P (1984) Milankovitch and climate Part 2. A sensitivity experiment to astronomical forcing with a spectral GCM: simulation of the annual cycle at 125,000 BP and 115,000 BP. D Reidel, Dordrecht, Holland, pp 733–763
- Schlesinger ME, Verbitsky M (1996) Simulation of glacial onset with a coupled atmospheric general circulation/mixed layer ocean – ice-sheet/asthenosphere model. *Paleoclimates* 2: 179–201
- Schlesinger WH, Andrews JA (2000) Soil respiration and the global carbon cycle. *Biogeochemistry* 48: 7–20
- Schmitz WJ, McCartney MS (1993) On the North Atlantic circulation. *Rev Geophys* 31: 29–49
- Shackleton NJ (1987) Oxygen isotopes, ice volume and sea level. *Quat Sci Rev* 6(3–4): 183–190
- Stocker TF (2000) Past and future reorganizations in the climate system. *Quat Sci Rev* 19: 301–319
- Stokes S, Thomas DSG, Washington R (1997) Multiple episodes of aridity in southern Africa since the last interglacial period. *Nature* 388: 154–158
- Sytus J, Gordon H, Chappell J (1994) Sensitivity of a coupled atmosphere-dynamic upper ocean GCM to variations of CO₂, solar constant, and orbital forcing. *Geophys Res Lett* 21(15): 1599–1602
- Verbitsky MY, Oglesby RJ (1992) The effect of atmospheric carbon dioxide concentration on continental glaciation of the Northern Hemisphere. *J Geophys Res* 97(D5): 5895–5909
- Weaver AJ, Eby M, Wiebe EC, Bitz CM, Duffy PB, Ewen TL, Fanning AF, Holland MM, MacFadyen A, Matthews HD, Meissner KJ, Saenko O, Schmittner A, Wang H, Yoshimori M (2001) The UVic Earth System Climate Model: model description, climatology, and applications to past, present and future climates. *Atmos Ocean* 4: 361–428

- Whitlock C, Bartlein PJ (1997) Vegetation and climate change in northwest America during the past 125 kyr. *Nature* 388: 57–61
- Wilson MF, Henderson-Sellers A (1985) A global archive of land cover and soils data for use in general circulation climate models. *J Climatol* 5: 119–143
- Yoshimori M, Reader MC, Weaver AJ, McFarlane NA (2002) On the causes of glacial inception at 116 ka BP. *Clim Dyn* 18: 383–402